Astronomy & Astrophysics manuscript no. manuscript_accepted
October 29, 2014
©ESO 2014

arXiv:1410.7602v1 [astro-ph.HE] 28 Oct 2014

Synchrotron Cooling in Energetic Gamma-Ray Bursts Observed by the *Fermi* Gamma-Ray Burst Monitor

Hoi-Fung Yu[1,2], Jochen Greiner[1,2], Hendrik van Eerten[1⋆], J. Michael Burgess[3,4], P. Narayana Bhat[5], Michael S. Briggs[5], Valerie Connaughton[5], Roland Diehl[1], Adam Goldstein[6], David Gruber[7], Peter A. Jenke[5], Andreas von Kienlin[1], Chryssa Kouveliotou[6], William S. Paciesas[8], Véronique Pelassa[5], Robert D. Preece[5,9], Oliver J. Roberts[10], and Bin-Bin Zhang[5]

[1] Max-Planck-Institut für extraterrestrische Physik, Giessenbachstraße 1, 85748 Garching, Germany
e-mail: sptfung@mpe.mpg.de
[2] Excellence Cluster Universe, Technische Universität München, Boltzmannstraße 2, 85748 Garching, Germany
[3] The Oskar Klein Centre for Cosmoparticle Physics, AlbaNova, SE-106 91 Stockholm, Sweden
[4] Department of Physics, KTH Royal Institute of Technology, AlbaNova, SE-106 91 Stockholm, Sweden
[5] Center for Space Plasma and Aeronomic Research (CSPAR), University of Alabama in Huntsville, 320 Sparkman Drive, Huntsville, AL 35805, USA
[6] Astrophysics Office, ZP12, NASA/Marshall Space Flight Center, Huntsville, AL 35812, USA
[7] Planetarium Südtirol, Gummer 5, 39053 Karneid, Italy
[8] Universities Space Research Association, 320 Sparkman Drive, Huntsville, AL 35805, USA
[9] Department of Space Science, University of Alabama in Huntsville, 320 Sparkman Drive, Huntsville, AL 35899, USA
[10] School of Physics, University College Dublin, Belfield, Dublin 4, Ireland

October 29, 2014

ABSTRACT

Context. In this paper we study the time-resolved spectral properties of energetic gamma-ray bursts (GRBs) with good high-energy photon statistics observed by the Gamma-Ray Burst Monitor (GBM) onboard the *Fermi* Gamma-Ray Space Telescope.
Aims. To constrain in detail the spectral properties of GRB prompt emission on a time-resolved basis and to discuss the theoretical implications of the fitting results in the context of various prompt emission models.
Methods. Our sample comprises eight GRBs observed by *Fermi* GBM in its first five years of mission, with 1 keV - 1 MeV fluence $f > 1.0 \times 10^{-4}$ erg cm^{-2} and signal-to-noise level S/N $\geq$ 10.0 above 900 keV. We perform time-resolved spectral analysis using a variable temporal binning technique according to optimal S/N criteria, resulting in a total of 299 time-resolved spectra. We fit the Band function to all spectra and obtain the distributions for the low-energy power-law index α, the high-energy power-law index β, the peak energy in the observed νF_ν spectrum E_p, and the difference between the low- and high-energy power-law indices $\Delta s = \alpha - \beta$. We also apply a physically motivated synchrotron model, which is a triple power-law with constrained power-law indices and a blackbody component, to test for consistency with a synchrotron origin for the prompt emission and obtain the distributions for the two break energies $E_{\mathrm{b},1}$ and $E_{\mathrm{b},2}$, the middle segment power-law index β, and the Planck function temperature kT.
Results. The Band function parameter distributions are $\alpha = -0.73^{+0.16}_{-0.21}$, $\beta = -2.13^{+0.28}_{-0.56}$, $E_\mathrm{p} = 374.4^{+307.3}_{-187.7}$ keV ($\log_{10} E_\mathrm{p} = 2.57^{+0.26}_{-0.30}$), and $\Delta s = 1.38^{+0.54}_{-0.31}$, with average errors $\sigma_\alpha \sim 0.1$, $\sigma_\beta \sim 0.2$, and $\sigma_{E_\mathrm{p}} \sim 0.1 E_\mathrm{p}$. Using the distributions of Δs and β, the electron population index p is found to be consistent with the "moderately fast" scenario which fast- and slow-cooling scenarios cannot be distinguished. The physically motivated synchrotron fitting function parameter distributions are $E_{\mathrm{b},1} = 129.6^{+132.2}_{-32.4}$ keV, $E_{\mathrm{b},2} = 631.4^{+582.6}_{-309.6}$ keV, $\beta = -1.72^{+0.48}_{-0.25}$, and $kT = 10.4^{+4.9}_{-3.7}$ keV, with average errors $\sigma_\beta \sim 0.2$, $\sigma_{E_{\mathrm{b},1}} \sim 0.1 E_{\mathrm{b},1}$, $\sigma_{E_{\mathrm{b},2}} \sim 0.4 E_{\mathrm{b},2}$, and $\sigma_{kT} \sim 0.1 kT$. This synchrotron function requires the synchrotron injection and cooling break (i.e., E_min and E_cool) to be close to each other within a factor of ten, often in addition to a Planck function.
Conclusions. A synchrotron model is found consistent with the majority of time-resolved spectra for eight energetic *Fermi* GBM bursts with good high-energy photon statistics, as long as both the cooling and injection break are included and the leftmost spectral slope is lifted either by inclusion of a thermal component or when an evolving magnetic field is accounted for.

Key words. gamma rays: stars - (stars:) gamma-ray burst: general - radiation mechanisms: non-thermal - methods: data analysis

1. Introduction

Gamma-ray bursts (GRBs) are the most luminous explosions in the Universe known to-date. The first GRB was discovered in 1967 (Klebesadel et al. 1973), and after over 45 years of research efforts it is now believed that GRBs originate from highly relativistic outflows from central compact sources at cosmological distances with bulk Lorentz factors $\Gamma > 100$ (e.g. Lithwick & Sari 2001; Hascoët et al. 2012). This is often understood in terms of the "fireball model" (Goodman 1986; Paczynski 1986; Rees & Meszaros 1992, 1994; Piran 1999), where the GRB itself is produced by dissipation of kinetic energy from the relativistic flow. However, the shape of GRB spectra does not naturally fit the synchrotron spectra predicted by this model. Even after many GRB dedicated missions, e.g. the Burst And Transient Source Explorer (BATSE, Fishman et al. 1989; Meegan et al. 1992) onboard the *Compton* Gamma-Ray Observatory (*CGRO*), the *Bep-*

⋆ Fellow of the Alexander v. Humboldt Foundation

Table 1. The names, GBM trigger numbers, durations, fluence, detectors used, and optimal S/N for the eight bursts studied in this paper.

GRB Name	GBM Trigger #	T_{90} (s)	f(1 keV - 1 MeV) (10^{-4}erg/cm^2)	NaI	BGO	S/N
090902B	090902.462	138.2±3.2	2.22±0.003	n0, n1, n9	b0	50
100724B	100724.029	114.7±3.2	2.17±0.006	n0, n1, n2	b0	40
100826A	100826.957	85.0±0.7	1.64±0.010	n7, n8	b1	30
101123A	101123.952	103.9±0.7	1.13±0.001	n9, na	b1	30
120526A	120526.303	43.6±1.0	1.16±0.002	n4	b0	20
130427A	130427.324	138.2±3.2	24.62±0.012	n6, na	b1	20
130504C	130504.978	73.2±2.1	1.29±0.002	n2, n9	b0	30
130606B	130606.497	52.2±0.7	2.01±0.002	n7, n8, nb	b1	40

poSAX satellite (Boella et al. 1997), the *Swift* satellite (Gehrels et al. 2004), and the *Fermi* Gamma-Ray Space Telescope (Atwood et al. 2009), no single consensus theory has emerged explaining all the features of the prompt emission, although various possibilities aside from the basic fireball model have been raised (see, e.g., Zhang 2014, for a recent overview).

To study the physical properties of GRB prompt emission, the observed γ-ray spectrum is usually fitted to a chosen model (either physical or empirical). Then the best fit parameters can be compared to the physical parameters used in theoretical models and computer simulations. Over the past 20 years the preferred fitting model has been the empirical Band function (Band et al. 1993), which consists of a smoothly joined broken power-law with low-energy power-law index α, high-energy power-law index β, and a characteristic energy $E_{\rm p}$ parameterized as the peak energy in the observed νF_ν spectrum.

Since the observed spectral behaviour varies from burst to burst and over time within a single burst, it is crucial to study the fitted parameters from a carefully selected sample of GRBs in a systematic way. Well-constrained spectral parameters are also important to distinguish among various theoretical models. However, due to the observed high-energy cutoff nature of the spectrum and the fact that it is harder to detect high-energy γ-ray photons, the high-energy power-law index is often poorly constrained for most bursts. Thanks to the broad spectral coverage of the Gamma-Ray Burst Monitor (GBM, Bissaldi et al. 2009; Meegan et al. 2009) onboard *Fermi*, we are now able to obtain the spectral indices with good precision.

Motivated by the fact that most catalog studies of large GRB samples do not consider the quality of high-energy photon statistics (e.g., Kaneko et al. 2006; Nava et al. 2011; Goldstein et al. 2012, 2013; Gruber et al. 2014; Yu et al. in prep.), we present time-resolved spectroscopy for eight energetic GRBs with good high-energy statistics in the GBM GRB zoo (Bissaldi et al. 2011) to obtain an accurate measurement of β. We describe the selection criteria, analysis procedures and empirical fitting models in Sect. 2. The observational results are presented in Sect. 3. We present the fitting results from the standard Band function in Sect. 3.1, and a test synchrotron model in Sect. 3.2. In Sect. 4 we discuss the theoretical implications of the observed parameter distributions in the context of different models. The conclusion is given in Sect. 5. Unless otherwise stated, all errors reported in this paper are given at the 1-σ confidence level.

2. GBM Data Analysis

2.1. Instrumentation

GBM is a sensitive scintillation array onboard the *Fermi* satellite. It consists of twelve thallium activated sodium iodide (NaI(Tl)) detectors covering energy from 8 keV to 1 MeV and two bismuth germanate (BGO) detectors covering energy from 200 keV to 40 MeV. This provides spectral coverage over three orders of magnitude, which makes GBM a powerful observing instrument for GRB prompt emission.

2.2. Burst, Detector, and Data Selection

The sample presented in this paper are among the most energetic bursts observed by *Fermi* GBM until 21 August 2013. They were selected according to two criteria: (1) total fluence in 1 keV - 1 MeV, $f > 1.0 \times 10^{-4}$ erg cm^{-2}; and (2) signal-to-noise level, S/N $\geq$ 10.0 above 900 keV (i.e. the NaI limit) in the BGO. The advantage of analysing bursts having significant photon statistics above 900 keV is that the high-energy power-law index can be better constrained. Moreover, high fluence provides more statistics for time-resolved spectral analysis. Table 1 lists the eight long GRBs (time in which 90% of burst fluence observed, $T_{90} > 2$ s) satisfying the above selection criteria. There are no short bursts in the sample because they do not satisfy our fluence criterion. GRB 130427A is the brightest burst observed by GBM. This brightness caused a pulse pile-up effect in the detectors in its complex-shaped main pulse after $t = T_0 + 2.4$ s. However, it also has a bright first pulse that is well suited for testing the synchrotron model (Preece et al. 2014) and that satisfies our selection criteria by itself. Therefore, this first pulse ($t < T_0 + 2.4$ s) is included in our analysis.

For each burst, up to three NaI detectors with viewing angle less than 60 degrees and the BGO without blockage by either the Large Area Telescope (Atwood et al. 2009) or the solar panels were included in order to maximize signals and reduce the level of background noise. We used the time-tagged event (TTE) data which provides high temporal (continuous temporal coverage with 2 μs time tags) and spectral resolution (128 pseudo-logarithmically scaled energy channels). The channels with energy less than 8 keV for NaIs and 245 keV for BGOs, together with the overflow channels, were excluded. As a result, an effective spectral range from 8 keV to 40 MeV was used in the analysis. Moreover, effective area corrections were applied to each pair of NaI and BGO detectors.

2.3. Time-Resolved Spectral Analysis

The light curves were binned using a fixed S/N for each burst (but varying across bursts, see last column of Table 1), in order to avoid artificial binning bias while preserving the general shape of the light curve by avoiding merging peaks and valleys (e.g. Guiriec et al. 2010), resulting in a total of 299 spectra. The binned light curves are shown in Figs. A.1 and A.2 with time relative to the GBM trigger time T_0.

Time-resolved spectroscopy was then performed with the GBM official spectral analysis software RMFIT[1] v4.3BA and the GBM response matrices v2.0. In order to account for the change in orientation of the source with respect to the detectors caused by the slew of the spacecraft, RSP2 files containing the detector response matrices (DRM) for every 2 degrees on the sky were used. For each burst a low-order polynomial (order 2 - 4) was fitted to every energy channel according to a user defined background interval before and after the prompt emission phase and interpolated across the emission interval.

Bhat (2013) reported that the typical minimum variability timescales (MVT) for short and long GRBs are 24 ms and 0.25 s respectively. The average temporal resolution of the time bins ($T_{\rm bin}$) used in this paper is 2.18 s, which is longer than the MVT. The pulse duration ($T_{\rm pulse}$) ranges from seconds to tens of seconds (see Figs. A.1 and A.2), which is, of course, by definition shorter than or equal to the burst duration T_{90}. So we have the typical values of MVT $< T_{\rm bin} < T_{\rm pulse} < T_{90}$.

The variable temporal S/N binning technique can avoid the resulting statistics being dominated by the brightest few bursts. This is because the optimal S/N for each burst is different which lead to similar number of bins for every bursts (see Tables A.1 - A.8). The fitting results will be given in Sect. 3 and discussed in Sect. 4. GRB 100724B will be discussed separately due to its ambiguous parameter distributions. We checked the statistics contributed by individual bursts and found that our conclusions are not affected if any one burst (even for GRB 100724B, see Sect. 3.1) is removed from the overall sample.

2.4. Empirical Fitting Models

2.4.1. Band Function (BAND)

The Band function (Band et al. 1993) was fitted to every spectrum:

$$f_{\rm BAND}(E) = A \begin{cases} \left(\frac{E}{100\,{\rm keV}}\right)^{\alpha} \exp\left[-\frac{(\alpha+2)E}{E_{\rm p}}\right] & \text{for } E < E_{\rm c}, \\ \left(\frac{E}{100\,{\rm keV}}\right)^{\beta} \exp\left(\beta-\alpha\right)\left(\frac{E_{\rm c}}{100\,{\rm keV}}\right)^{\alpha-\beta} & \text{for } E \geq E_{\rm c}, \end{cases} \tag{1}$$

where

$$E_{\rm c} = \left(\frac{\alpha-\beta}{\alpha+2}\right) E_{\rm p}. \tag{2}$$

In the above equations, A is the normalization factor at 100 keV in units of photons s^{-1} cm^{-2} keV^{-1}, α is the low-energy power-law index, β is the high-energy power-law index, and $E_{\rm p}$ is the peak energy in units of keV in the observed νF_ν spectrum. The energy $E_{\rm c}$ is where the low-energy power-law with an exponential cutoff ends and the pure high-energy power-law starts.

2.4.2. Synchrotron Model (SYNC)

The optically thin Synchrotron Shock Model (SSM) predicts two different spectra, "fast-cooling" and "slow-cooling" (e.g. Sari et al. 1998; Preece et al. 2002), depending on the injection and evolution of the relativistic electron population. Both of them consist of a lower and a higher frequency break, fixed by the values of the cooling frequency $\nu_{\rm cool}$ and the minimum injection frequency $\nu_{\rm min}$ for the relativistic electrons. The electrons in the shock are accelerated to a minimum energy $\gamma_{\rm min}$. Assuming a power-law behaviour for the electron energy distribution $N(\gamma_{\rm e}) \propto \gamma_{\rm e}^{-p}$, where $\gamma_{\rm e} \geq \gamma_{\rm min}$ is the electron energy, the emission spectrum also has a power-law shape. As long as $p > 2$, the distribution is characterized by its lower cut-off at $\gamma_{\rm min}$, and the integrated energy of the population does not diverge at high electron energies.

There is a critical energy $\gamma_{\rm cool}$ such that electrons with energies above $\gamma_{\rm cool}$ emit a significant amount of their energy via synchrotron cooling. The values of $\gamma_{\rm cool}$ and $\gamma_{\rm min}$ correspond to $\nu_{\rm cool}$ and $\nu_{\rm min}$ respectively, and the slow-cooling spectrum is given by

$$F_{\nu,{\rm slow}} \propto \begin{cases} \nu^{1/3} & \text{for } \nu_{\rm min} > \nu, \\ \nu^{-(p-1)/2} & \text{for } \nu_{\rm cool} > \nu > \nu_{\rm min}, \\ \nu^{-p/2} & \text{for } \nu > \nu_{\rm cool}, \end{cases} \tag{3}$$

while the fast-cooling spectrum is given by

$$F_{\nu,{\rm fast}} \propto \begin{cases} \nu^{1/3} & \text{for } \nu_{\rm cool} > \nu, \\ \nu^{-1/2} & \text{for } \nu_{\rm min} > \nu > \nu_{\rm cool}, \\ \nu^{-p/2} & \text{for } \nu > \nu_{\rm min}. \end{cases} \tag{4}$$

Subtracting 1 from the spectral indices will give the photon indices (i.e. α and β) which will be obtained in Sect. 3, leading to a synchrotron "line-of-death" $\alpha = -2/3$ for both scenarios and a second line-of-death $\alpha = -3/2$ (Preece et al. 1998) for the fast-cooling scenario. Figure 1 shows the schematic spectra for the slow- and fast-cooling scenario as well as the so-called "both" case where $\nu_{\rm cool}/\nu_{\rm min}$ (slow-cooling) or $\nu_{\rm min}/\nu_{\rm cool}$ (fast-cooling) is close to unity. The "both" case can be considered to describe an intermediate case of "moderately fast-cooling".

The synchrotron fitting model that we apply is a modified triple power-law with sharp breaks defined as:

$$f_{\rm SYNC}(E) = A \begin{cases} \left(\frac{E}{100\,{\rm keV}}\right)^{\alpha} & \text{for } E < E_{\rm b,1}, \\ \left(\frac{E_{\rm b,1}}{100\,{\rm keV}}\right)^{\alpha-\beta}\left(\frac{E}{100\,{\rm keV}}\right)^{\beta} & \text{for } E_{\rm b,1} \leq E < E_{\rm b,2}, \\ \left(\frac{E_{\rm b,1}}{100\,{\rm keV}}\right)^{\alpha-\beta}\left(\frac{E_{\rm b,2}}{100\,{\rm keV}}\right)^{\beta-\gamma}\left(\frac{E}{100\,{\rm keV}}\right)^{\gamma} & \text{for } E \geq E_{\rm b,2}, \end{cases} \tag{5}$$

where A is the normalization factor at 100 keV in units of photons s^{-1} cm^{-2} keV^{-1}, α, β, and γ are the power-law indices of the three segments (from low to high energies), and $E_{\rm b,1}$ and $E_{\rm b,2}$ are the two break energies in units of keV. Here we fixed $\alpha = -2/3$ and $\beta - \gamma = 1/2$ to create a SYNC-slow model (Eqn. 3). This makes it a four parameter model with freely varying A, $E_{\rm b,1}$, $E_{\rm b,2}$, and β (or equivalently, γ). We also tried to fit the SYNC model with fixed $\alpha = -2/3$ and $\beta = -3/2$ to create a SYNC-fast model (Eqn. 4). This also makes a four parameter model with freely varying A, $E_{\rm b,1}$, $E_{\rm b,2}$, and γ.

2.4.3. Blackbody Model (BB)

We also added a blackbody model to the SYNC fits. It is a Planck function defined as:

$$f_{\rm BB}(E) = A\left[\frac{(E/1\,{\rm keV})^2}{\exp(E/kT)-1}\right], \tag{6}$$

where A is the normalization factor at 1 keV in units of photons s^{-1} cm^{-2} keV^{-1} and kT is the temperature of the blackbody in units of keV.

[1] The public version of the RMFIT software is available at http://fermi.gsfc.nasa.gov/ssc/data/analysis/rmfit/

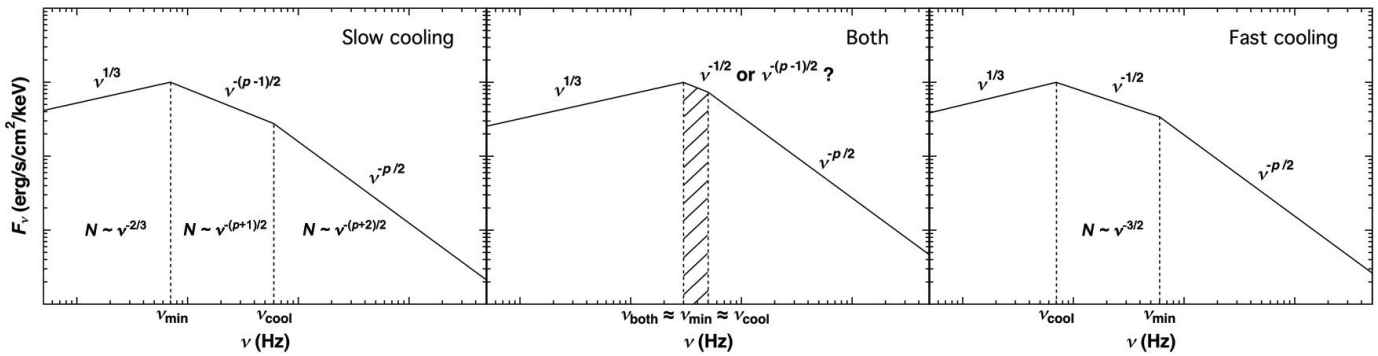


Fig. 1. Schematic spectra for the SSM cooling scenarios. The left, middle, and right panels show the "slow", "both", and "fast" cases in the energy flux space, respectively. The shaded region represents the possible location of $\nu_{\rm both}$ (i.e. $E_{\rm p}$) when fitting the observed spectrum using a model with smoothly jointed power-laws. The photon distribution slopes are also indicated for each different case.

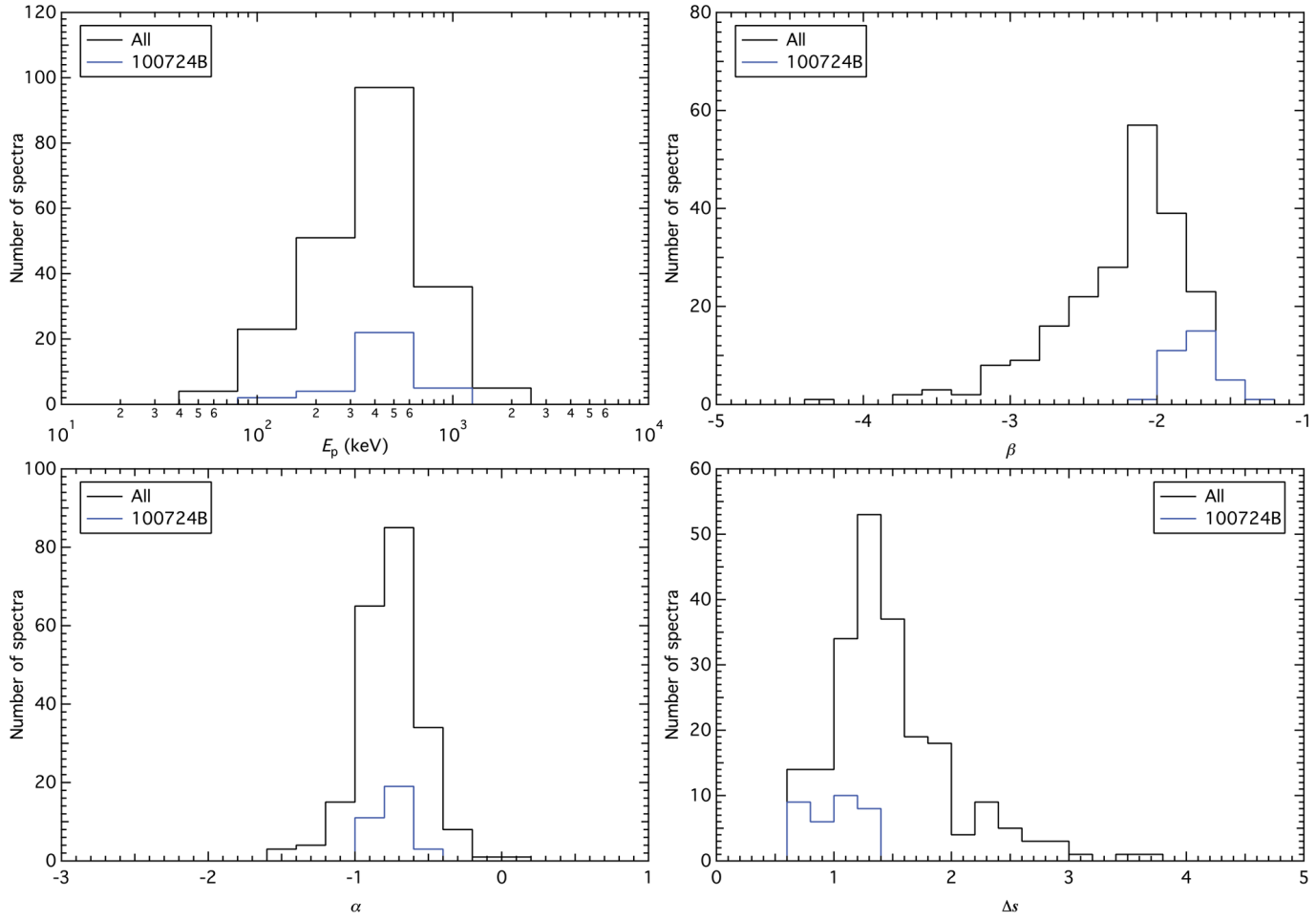


Fig. 2. Distributions of the constrained parameters obtained from the BAND model. The upper left panel shows the distributions of the values of $E_{\rm p}$. The lower left panel shows the distributions of the values of α. The upper right panel shows the distributions of the values of β. The lower right panel shows the distributions of the values of $\Delta s = \alpha - \beta$. The blue lines show the distributions of GRB 100724B.

3. Fitting Results

3.1. BAND Fits

The Band function has long been known to provide a good fit to prompt emission spectra (Band et al. 1993), where the typical reduced-$\chi^2 \approx 1$ (there is a caveat that the χ^2 statistics may not be suitable for non-Gaussian data) and the Castor C-Statistics values (CSTAT, Cash 1979) are low (often a few hundred to a thousand for GBM fits depending on the data quality of individual burst) among the simplest models (e.g. Goldstein et al. 2012; Gruber et al. 2014; Yu et al. in prep.). If, in addition to a low CSTAT value corresponding to a low reduced-χ^2 value ($\approx$ 1), all parameters in an individual spectral fit have 1-σ relative error $\sigma_{\rm parameter}$/(parameter value) < 1.0 (for power-law indices we use absolute error $\sigma_{\rm parameter} < 1.0$), we define the fit as a constrained fit. For all these good fits, we verify that the data points

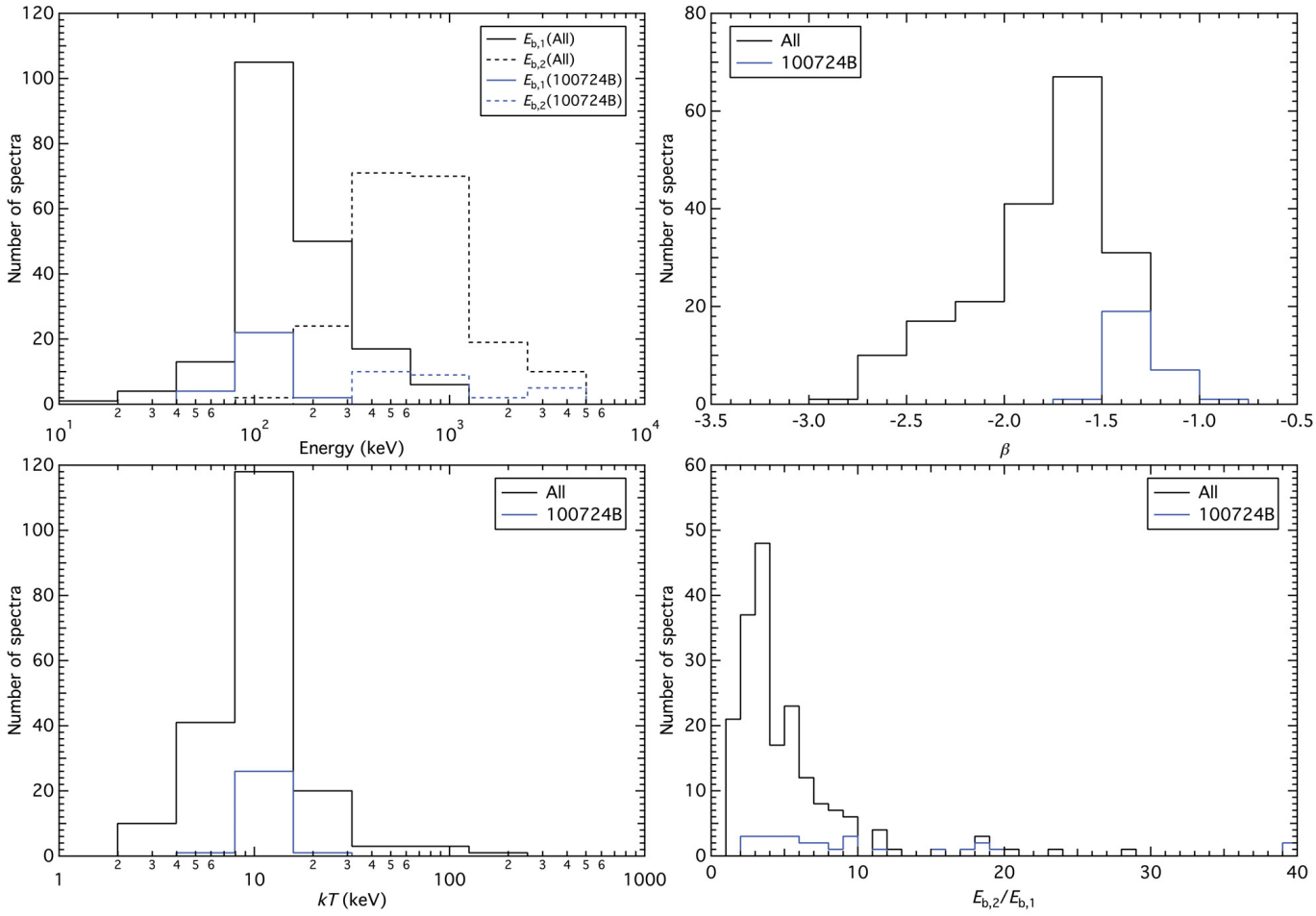


Fig. 3. Distributions of the constrained parameters obtained from the SYNC+BB model with slow-cooling constraints (i.e. $\alpha = -2/3$ and $\beta - \gamma = 1/2$). The upper left panel shows the break energies $E_{b,1}$ and $E_{b,2}$. The lower left panel shows the kT distribution. The upper right panel shows the photon indices β of the middle power-law segment. The lower right panel shows the ratio between the two breaks, $E_{b,2}/E_{b,1}$. The blue lines show the distributions of GRB 100724B. Values that are out of the plotting region are accumulated in the boundary bins.

are within $\approx 99.73\%$ confidence level to the model curves. Although we found that in some extreme cases the asymmetric errors of β may be unconstrained on the negative side, our selection criteria can filter most of these cases by ensuring the symmetric error (which is the mean of the asymmetric errors) to be well behaved. As a result, 216 of the total 299 spectra ($\approx 72\%$) are constrained. Figure 2 shows the distributions of the constrained parameters for the BAND model: the low-energy power-law index α, the high-energy power-law index β, the peak energy in the observed νF_ν spectrum E_p, and the difference between the low- and high-energy power-law indices $\Delta s \equiv \alpha - \beta$.

The distributions of α, β, E_p, and Δs are clustered around values of $-0.73^{+0.16}_{-0.21}$, $-2.13^{+0.28}_{-0.56}$, $374.4^{+307.3}_{-187.7}$ keV ($\log_{10} E_\mathrm{p} = 2.57^{+0.26}_{-0.30}$), and $1.38^{+0.54}_{-0.31}$, respectively. The asymmetric distribution errors were determined via taking the difference between the median values of the cumulative distribution function (CDF) and the 68% quantiles. Note that $\alpha = -0.73^{+0.16}_{-0.21}$ shows that the overall sample distribution is consistent with the synchrotron line-of-death (see Sect. 2.4.2). About a third of the individual spectra are consistent with the value $\alpha = -2/3$ within 1-σ. The slope $\beta = -2.13^{+0.28}_{-0.56}$ is consistent with typically observed values. The average errors of α and β are $\sigma_\alpha \sim 0.1$ and $\sigma_\beta \sim 0.2$, respectively. So in Fig. 2 a bin width equals to 0.2 was chosen for displaying the histograms. This implies that the observed dispersions in the power-law index distributions cannot be explained solely by statistical uncertainties. The dispersion is also observed within bursts, indicating that spectral evolution has a non-negligible effect on the parameter distribution. Moreover, it is observed that $\sigma_{E_\mathrm{p}} \sim 0.1 E_\mathrm{p}$.

The distribution of E_p peaks at $374.4^{+307.3}_{-187.7}$ keV and are only slightly higher than those found in the GBM time-averaged spectral catalogs (Goldstein et al. 2013; Gruber et al. 2014) and the BATSE spectral catalogs (e.g. Kaneko et al. 2006). According to Fig. 2, 91% of all $E_\mathrm{p} \leq 1$ MeV. The remaining 9% has the highest $E_\mathrm{p} = 2.1$ MeV (GRB 130504C, see Table A.7). Nava et al. (2011) presented a time-averaged spectral analysis on 44 short GBM GRBs, and found that the distribution peaks at $E_\mathrm{p} = 500^{+260}_{-175}$ keV. This suggests that our long bursts could be as hard as short bursts, which is expected since we selected the bursts with relatively better statistics in the BGO channels. Our bursts lie at the high E_p-long T_{90} end in the long/soft-short/hard classification of GRBs (Kouveliotou et al. 1993). However, it should be noted that the brightest three short GBM GRBs show E_p as large as 6 MeV (Guiriec et al. 2010). This shows that the E_p dispersion within long or short bursts can also be huge. In addition, E_p is observed to be decreasing throughout a burst, with intensity-tracking behaviour during sub-pulses within a single burst (see Sect. 4.1).

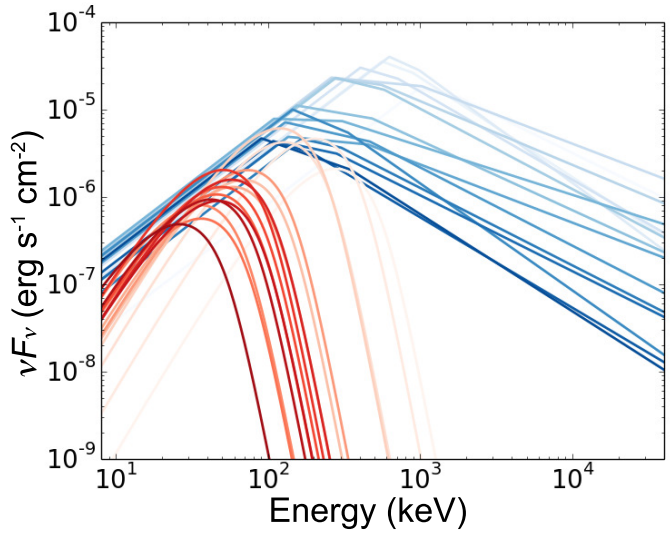


Fig. 4. The νF_ν spectral evolution of the SYNC-slow model for GRB 130427A. The evolution of the SYNC component evolves from cyan to blue, while the BB component evolves from yellow to red. No clear correlation is found between the two components.

As shown in Fig. 2, 50% of the hard $\beta > -2$ are from GRB 100724B. We will show in Sect. 4.2 that this burst is consistent with both the slow- and fast-cooling scenario, and that the general conclusion is not affected beacuse removing this burst will only make the distribution peak narrower.

3.2. SYNC Fits

Various studies have shown that a thermal component around a few times 10 keV may generally exist (e.g. Mészáros et al. 2002; Ryde 2005; Guiriec et al. 2011; Axelsson et al. 2012; Guiriec et al. 2013; Burgess et al. 2014a,b). In addition, Burgess et al. (2014a) showed that a SYNC type model alone cannot be reconciled with the flatness of α. We found that in most of our spectra adding a blackbody component can greatly improve the fit. Therefore, all the spectra were fit again to include a blackbody component in the SYNC model. The theoretical implications for the SYNC+BB and BAND model are discussed in Sect. 4.

Two SYNC+BB models (i.e. SYNC-slow+BB and SYNC-fast+BB) were fitted to all spectra using a customized version of RMFIT. We validated that these are good fits to the data by various goodness-of-fit measures: (1) reduced-χ^2 values are close to unity; (2) CSTAT values are comparable to, often lower than, those for the BAND fits (e.g. Gruber et al. 2014; Burgess et al. 2014a); and (3) quantile-quantile plots for the cumulative observed vs. model count rates lie very close to $x = y$, thus confirming that a SYNC+BB model description is consistent with the data. For reference, the CSTAT values for all spectra are listed together with the degrees of freedom (DOF) and the fitted parameters in Tables A.1 - A.8. It is found that both the SYNC-slow+BB and -fast+BB models provide constrained fits in more than 65% of all spectra. We show in Sect. 4 that such a test model can provide constraints on various prompt emission mechanism theories. The distributions for the SYNC-slow+BB constrained parameters are plotted in Fig. 3. The time-resolved spectral evolution for GRB 130427A is shown in Fig. 4. There is no clear correlation found between the fluxes of the SYNC and BB components.

The upper left panel of Fig. 3 shows the distributions of $E_{\rm b,1}$ and $E_{\rm b,2}$. We found that there are two clear peaks for the breaks around $129.6^{+132.2}_{-32.4}$ keV and $631.4^{+582.6}_{-309.6}$ keV for $E_{\rm b,1}$ and $E_{\rm b,2}$, respectively. The asymmetric distribution errors were obtained via the same procedure by constructing CDFs as described in Sect. 3.1. Comparing to the BAND fits, it is observed in most of the cases that $E_{\rm b,1} < E_{\rm p} \approx E_{\rm b,2}$. We found that 100% of $E_{\rm b,1} <$ 1 MeV and 97% of $E_{\rm b,2} <$ 3 MeV.

The lower left panel shows the kT distribution. The parameter distribution of $kT = 10.4^{+4.9}_{-3.7}$ keV creates a bump at $\sim$ 30 keV. This kT distribution is consistent with most of the sub-dominant thermal bursts observed (e.g. Ryde 2005; Guiriec et al. 2011; Axelsson et al. 2012; Guiriec et al. 2013; Burgess et al. 2014a,b). When the Planck-to-SYNC flux ratio is high, the Planck function dominates the curvature of the lowest end of the spectrum.

The upper right panel shows the distribution of β, where $\beta - \gamma = 1/2$. The parameter distribution of $\beta = -1.72^{+0.48}_{-0.25}$ translates to the electron distribution index $p = 2.44^{+0.50}_{-0.96}$. A synchrotron spectrum with $p > 2$ (i.e. $\beta < -1.5$) requires no upper cut-off in order for the total energy of the electrons to remain finite (Sect. 2.4.2). Therefore, the measured high-energy slopes for SYNC model do not require such a cut-off to exist. In addition, this is also consistent with afterglow-deduced distributions of $p \sim 2.3$ (e.g., Curran et al. 2010; Ryan et al. 2014). GRB 100724B provided most of the cases where $\beta > -1.5$, which matches the fast-cooling index value.

The lower right panel shows the distribution of the ratio between the two breaks, $E_{\rm b,2}/E_{\rm b,1}$. It is observed that $E_{\rm b,2}$ and $E_{\rm b,1}$ have a peak ratio at $3.77^{+4.01}_{-1.53}$, and over 90% are below 10. If we assume $E_{\rm b,1}$ and $E_{\rm b,2}$ are related to $E_{\rm min} = h\nu_{\rm min}$ and $E_{\rm cool} = h\nu_{\rm cool}$, then a ratio of $E_{\rm b,2}/E_{\rm b,1} < 10$ poses a very tight constraint on the theoretical models (see Sect. 4.3).

The parameter distributions for the SYNC-fast model are nearly identical to those of the SYNC-slow model (which is expected because the value of $\beta = -3/2$ is only 0.1 away from the SYNC-slow β distribution peak). The only difference observed is that γ extends to much steeper values (from -1.75 to -4.50 with a peak around -2.0 - -2.5, not a normally distributed population), which reflects the fact that since the power-law segments are no longer connected, γ can go much steeper in the time bins that contain mostly upper limits in the high-energy channels.

In brief, the following features are observed in the SYNC fits: (1) over 90% of $E_{\rm b,2}/E_{\rm b,1} < 10$; (2) a bump/flattening feature at $\sim$ 30 keV; and (3) a general hard-to-soft evolution for the peak/break energy is observed. We discuss the theoretical implications of these observational results in the next section.

4. Theoretical Implications

4.1. Hard-to-Soft Evolution and Intensity-Tracking Behaviour

We show the light curves overlaid on the evolutions of $E_{\rm p}$, $E_{\rm b,1}$, $E_{\rm b,2}$, and kT for every burst in Figs. A.1 and A.2. Hard-to-soft evolution over the whole bursting period is observed in every burst with in-pulse intensity-tracking behaviour. These two modes of evolutionary trend have been observed in many GRBs (e.g., Ford et al. 1995; Liang & Kargatis 1996; Kaneko et al. 2006; Preece et al. 2000; Guiriec et al. 2010; Lu et al. 2010; Peng et al. 2010; Ghirlanda et al. 2011; Burgess et al. 2014a; Preece et al. 2014). Hard-to-soft evolution is a natural prediction from the SSM (Daigne & Mochkovitch 1998), in which the relative Lorentz factors of the colliding shells become lower and the spectra become softer. For instance, Lu et al. (2012) reported a time-resolved spectral analysis for 62 *Fermi* bursts (51

long + 11 short) with a detailed study of the $E_{\rm p}$ evolution. They found that the two modes for $E_{\rm p}$ evolution are present in different pulses and in different bursts. Despite the complexity of the issue, they suggested that the intensity-tracking behaviour could be at least partially attributed to the superposition of hard-to-soft pulses in a highly superimposed light curve. As all bursts in our sample are multi-pulsed (though for GRB 130427A only the first pulse is analyzed, see Sect. 2.2), this possibility cannot be excluded. We also observed that the $E_{\rm p}$ in later pulses never gets as high as in the first pulse, even if a later pulse has a higher peak flux. This suggests that the hard-to-soft evolution dominates over the intensity-tracking behaviour, and that the hard-to-soft evolution is an intrinsic property of GRBs with intensity-tracking behaviour added on top.

4.2. Synchrotron Emission and the Band Function Fits

The values of Δs and β obtained from the BAND fits can be used to compute the electron distribution power-law index p and to distinguish among different cooling scenarios (Preece et al. 2002). Preece et al. (2002) performed time-resolved spectroscopy on 156 BATSE GRBs and found that the results are consistent with the "slow, low", "both", or "fast, high" cases (with "low" and "high" referring to just the lower or higher spectral break respectively).

The relative rate of electron cooling against energy injection into the electron population marks the difference between slow- and fast-cooling. To obtain the synchrotron cooling and energy injection timescale requires knowledge of the physical parameters of the ejecta, e.g. magnetic field strength and electron Lorentz factor, as well as precise modelling of the energy output from the central engine. This makes accurate measurements of these timescales difficult. In the internal shock model, the relative Lorentz factors between colliding shells are only mildly relativistic (Daigne & Mochkovitch 1998), and the synchrotron cooling timescale of the relativistic electrons in the ejecta frame is

$$t_{\rm syn} = 6\left(\frac{\Gamma_{\rm e}}{100}\right)^{-1}\left(\frac{B}{1000\ {\rm G}}\right)^{-2}\ {\rm s}, \tag{7}$$

where $\Gamma_{\rm e}$ is the Lorentz factor of the electrons relative to the ejecta and B is the magnetic field in the shock. One could compare, for instance, $t_{\rm syn}$ with the MVT observed in the light curve (as experienced in the ejecta frame), which is then taken to represent the rate of energy injection into the synchrotron electron population. However, the inferred values of the physical parameters, such as magnetic field strength (see the discussion below), vary in a wide range among bursts and sub-pulses within a single bursts. Taken together with the uncertainty in the spatial and temporal profile of the particle acceleration sites (e.g. extended turbulent regions vs. shock acceleration, or intermittent vs. continuous injection), it becomes hard to predict a clear preference for a given cooling regime due to the difficulty of unambiguously interpreting the observable time scales. We show in the following that a mix of both the slow- and fast-cooling is implied by the GBM data.

Table 2 shows the values of p obtained from the Δs and β distributions (see Eqns. 8 - 12 in Preece et al. 2002). Column 1 shows the three cases where p depends on both Δs and β. Column 2 shows the respective value of α in each case. Columns 3 and 6 show the formulae for p as a function of Δs and β respectively. Columns 4 and 7 give the ranges of possible values of p calculated from the distributions of Δs and β for all eight bursts, and Cols. 5 and 8 give the same for GRB 100724B alone.

It can be seen that the values of p in Col. 4 are inconsistent with the "fast, high" case in Col. 7. The "fast, low" case predicts $\Delta s = 5/6$ which is clearly rejected as shown in Fig. 2. The distribution of fast-cooling $\gamma_{\rm SYNC}$ as mentioned in Sect. 3.2 indicates that the electron distribution index above $\gamma_{\rm min}$ can take any value from p = 1.5 - 6.0. Theories of electron shock-acceleration typically predict p values between 2 and 3, which makes these very steep values for p suggestive of the presence of a cut-off or deviation from a power-law slope in the accelerated particle distribution, rather than a single very steep slope. A steep electron distribution index can also occur when the shock normal is at an angle to the magnetic field, allowing electrons to escape the acceleration region early (Ellison & Double 2004; Baring 2006; Summerlin & Baring 2012; Burgess et al. 2014a). The "slow, high" case, which refers to the higher energy break in the left panel of Fig. 1, predicts $\Delta s = 1/2$ and is clearly rejected as shown in Fig. 2. The average values of Δs and β for GRB 100724B are 1.0 and -1.7 respectively, which are also consistent with the "slow, low" and "both" cases (Cols. 5 and 8), at the same time consistent with the "fast, low" case which predicts $\Delta s = 5/6$.

On the other hand, the BATSE β and Δs distributions suggested that the "slow, low", "fast, low", and "both" cases are all viable processes (see, e.g., Fig. 2 of Preece et al. 2002; Kaneko et al. 2006). Gruber et al. (2014) also showed similar conclusions in the GBM time-averaged spectra. Burgess et al. (2014a) performed a Bayesian time-resolved spectral analysis using physical synchrotron and thermal models instead of the Band function to several GBM GRBs and found that the slow-cooling scenario is a better explanation to the observed data, and their results suggest continuous energy injection is important. Uhm & Zhang (2014) predicted that using a decaying magnetic field as a function of radius, with a decay index b, it is possible for most GRBs to cool via the fast-cooling scenario with $\alpha \sim -1.0$. They predicted that the asymptotic value of the low-energy electron distribution should be $p = (6b-4)/(6b-1)$ instead of $p = 2$ for a constant magnetic field (e.g. Preece et al. 2002), and the spectral index $s = (-p+1)/2 = 3/(12b-2) = \alpha+1$. We found that in more than 77% of the constrained fits b has values between 0.6 and 2.6. There is no clear evolutionary trend of b. The variability of b within bursts is difficult to reconcile with a large scale power-law dependence on radius of the magnetic field. However, this can still be the case, but just not as clearly manifested in the data as predicted by Uhm & Zhang (2014).

In brief, our results are consistent with slow-cooling with the low-frequency break seen (or in the "both" case, undistinguished between slow- and fast-cooling). In the case of GRB 100724B, fast-cooling is also consistent with the low-frequency break seen. This implies that the second line-of-death, $\alpha = -3/2$, could also be avoided.

4.3. Synchrotron Models Fits

The SYNC-slow model is basically a three-segment broken power-law, with the middle- and high-energy segment connected (i.e. $\beta_{\rm SYNC} - \gamma_{\rm SYNC} = 1/2$). It is essentially an extended version of the BAND model, in which the curvature of BAND is replaced by two breaks and the power-law segment in between. This implies that when we are comparing the results from BAND and SYNC fits, it should be kept in mind that either $\beta_{\rm SYNC}$ or $\gamma_{\rm SYNC}$ could be picking up $\beta_{\rm BAND}$. This is discussed later in the current subsection. It should also be noted that a sharply joined broken power-law is intrinsically non-physical. The actual spectrum should always be smooth, so sharp power-law fits run the risk of covering a single smooth transition with multiple sharp breaks.

Table 2. Electron distribution index p for different cases.

Case[a]	α	$p = f(\Delta s)$	$f(1.2)$ - $f(1.6)$[b]	$f(1.0)$[c]	$p = g(\beta)$	$g(-2.0)$ - $g(-2.4)$[b]	$g(-1.7)$[c]
(1)	(2)	(3)	(4)	(5)	(6)	(7)	(8)
Fast, high...	$-3/2$	$2\Delta s + 1$	3.4 - 4.2	3.0	$-2(\beta + 1)$	2.0 - 2.8	1.4
Slow, low...	$-2/3$	$2(\Delta s + 1/6)$	2.73 - 3.53	2.33	$-2\beta - 1$	3.0 - 3.8	2.4
Both.....	$-2/3$	$2(\Delta s - 1/3)$	1.73 - 2.53	1.33	$-2(\beta + 1)$	2.0 - 2.8	1.4

Notes. [(a)] Preece et al. (2002), Eqns. (9), (10), and (12). [(b)] Calculated from the ranges of peak and average values of Δs and β distributions for all eight bursts, given that $1.2 < (\Delta s)_{\rm peak} < 1.4$, $1.4 < (\Delta s)_{\rm average} < 1.6$, $-2.2 < \beta_{\rm peak} < -2.0$, and $-2.4 < \beta_{\rm average} < -2.2$. [(c)] Calculated from the average values of Δs and β distributions for GRB 100724B only.

However, a smoothly joined triple power-law would contain too many parameters and to fit such a complicated empirical model is statistically unsound. The constrained power-law indices in our SYNC-slow and -fast models mitigate the issue by assuming a synchrotron origin of the observed spectrum a priori, thereby limiting the possible shapes of fitted spectra.

Theoretically, the SYNC model has excluded the synchrotron emission from Maxwellian electrons. This is because we wanted to have the synchrotron emission occurring at the right frequencies (i.e. γ-rays), which requires the energy per emitting electron to be higher than that obtained by simply averaging (as demonstrated by Daigne & Mochkovitch 1998). This implies a small subset of electrons at very high energies, far away from the thermal pool from which they were drawn. Alternatively, if the Maxwellian electron distribution peak and the minimum injection Lorentz factor (i.e. $\gamma_{\rm min}$) remain close, the effect of adding the Maxwellian electrons will be a smoothening of the synchrotron function that we could not model by our BAND or SYNC models. Moreover, Burgess et al. (2011) has shown that the Maxwellian electron population is sub-dominant. Thus in order to avoid further complication of the fitting model, we assume the synchrotron emission is just from the population of shock-accelerated electrons (see Sect. 3.2). However, one should note also that the Maxwellian does not just have to exist as left over thermal pool from the thermal parts of the jet. It can also be created in the shock region due to thermalization of electrons crossing the shock (see, e.g., Spitkovsky 2008).

According to the SYNC-slow fitting results, there are two cases to consider: (1) the $\gamma_{\rm SYNC}$ is the high-energy segment in the slow cooling scenario, i.e. $\nu_{\rm min}$ and $\nu_{\rm cool}$ are the predicted break values; or (2) $\gamma_{\rm SYNC}$ is the middle-energy segment in the slow-cooling scenario, in this case the triple power-law is just mimicking the slowly varying BAND model. If (1) is true, then we can take $\gamma_{\rm SYNC} = -2.5$ - -2.0, and we will have $p = 2.0$ - 3.0. Looking at Table 2, it can be seen that the SYNC-slow model is consistent with the "both" case; if (2) is true, then instead of comparing to $\gamma_{\rm SYNC}$, we should compare with $\beta_{\rm SYNC}$ in Eqn. 3, and we will have $p = 3.0$ - 4.0. Looking at Table 2, it can be seen that the SYNC-slow model is also consistent with the "slow, low" case.

Burgess et al. (2014a) used a physical non-thermal plus thermal synchrotron kernel to fit a few GBM GRBs and found that slow-cooling is physically possible. Since the typically observed value of $\alpha \sim -1.0$, the fast-cooling model has been disfavoured as it predicts α should be as steep as $-3/2$ below $\nu_{\rm min}$ (Sari et al. 1998). The presence of a blackbody contribution to the lower part of the spectrum would render it even more difficult to reconcile the α slope with the "fast, high" case. On the one hand, our fit results for the SYNC-slow model yield p values closer to the expected range between 2 and 3. On the other hand, a SYNC-fast model, implying that most of the energy of the electrons is radiated away, has the advantage of allowing for a lower efficiency. The total energy in γ-rays is typically comparable to the inferred kinetic energy of the ejecta. Therefore, if the efficiency in converting accelerated electron energies to radiation is low, the efficiency in extracting energy from the ejecta to the non-thermal electron population has to become extremely high in order to compensate (see e.g. Nousek et al. 2006; Granot et al. 2006, for detailed discussions). The fact that in the SYNC fits, both spectral breaks consistently occur fairly close to one another, does alleviate the issue, in that it provides essentially a "moderately fast-cooling" scenario, regardless of the precise order of the breaks. This, however, begs the question how to understand the universal break ratio between $\nu_{\rm min}$ and $\nu_{\rm cool}$ inferred from our sample, as the positions of these breaks are not theoretically expected to be related.

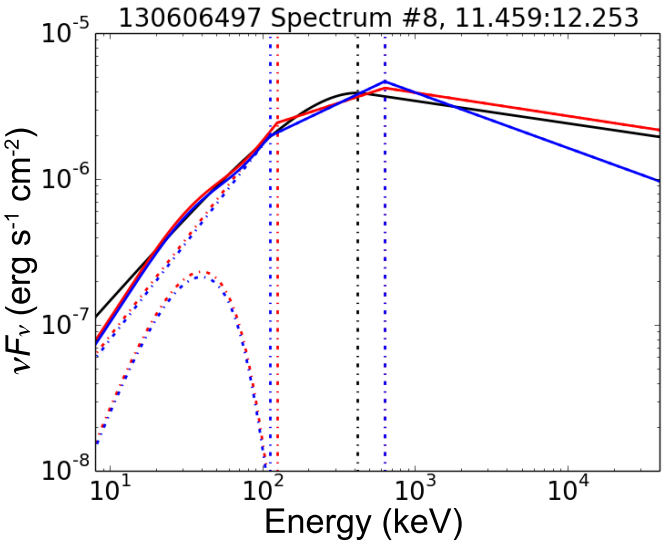


Fig. 5. A selected spectrum from GRB 130606B plotted in νF_ν space. The black, red, and blue solid curve show the fitted spectrum for the BAND, SYNC-slow+BB, and SYNC-fast+BB model, respectively, while the dash-dotted curves show individual SYNC or BB component. The vertical dash-dotted black, red, and blue line show the $E_{\rm p}$ and break energies for the BAND, SYNC-slow+BB, and SYNC-fast+BB model, respectively.

The fast-cooling model with a decaying magnetic field (Uhm & Zhang 2014) predicts a Band function spectral shape with $b \sim 1.0$ - 1.5 (see their Fig. 4), in which the curved Band shape is a sum-up effect for the emissions of electrons at different times. A decay index $b \lesssim 2.6$ (see Sect. 4.2) implies stronger magnetic dissipation and the electrons at later time could be cooled via slow-cooling, thus the positions of $\nu_{\rm cool}$ and $\nu_{\rm min}$ could reverse and move closer to each other, so that the "both" case is possible. Uhm & Zhang (2014) showed that this is possible in a

timescale $\sim$ 1.0 s, consistent with the typical $T_{\rm bin}$ used in this paper (see Sect. 2.3). We found that the BAND and SYNC model have extremely similar shapes (Fig. 5), consistent with this interpretation and thus providing further support for the "both" case.

4.4. Thermal Origin of Prompt Emission

Recently, Beloborodov (2013) suggested that the evolution of $E_{\rm p}$ could be a manifestation of thermal emission. As shown in Fig. 2, more than 90% of $E_{\rm p}$ values remain below 1 MeV. The observed clustering of $E_{\rm p}$ $\sim$ few hundred keV, instead of a wide distribution, is hard to explain in the SSM. The observed spectral width in the νF_ν space, is $\log(E_1/E_2) \approx 1.0$ - 1.5 decades in photon energy (Beloborodov 2013), where $E_2 - E_1$ is the width at half-maximum. This is narrower than a synchrotron model would predict (Daigne et al. 2011).

Early photospheric models assumed a freely expanding radiation-dominated outflow with no baryonic loading or magnetic field (Goodman 1986; Paczynski 1986). This predicts a sharply defined peak with a Planck spectrum (Beloborodov 2011), which is in contradiction to the observed non-thermal spectra in most GRBs. Detailed radiation transfer simulations have shown that a thermal origin of the Band function is possible (Pe'er et al. 2006; Giannios 2008; Beloborodov 2010; Vurm et al. 2011), and Beloborodov (2013) computed that the maximum $E_{\rm p}$ of a spectrum from thermal plasma is given by $30\Gamma_{\rm P}$ keV under high radiation efficiency, where $\Gamma_{\rm P}$ is the Lorentz factor of the Planckian photospheric shell. With the typical values of the Lorentz factor of GRBs to be $\sim$ 100, $E_{\rm p,max} \sim 3$ MeV in the rest frame. This value is consistent with most of our observed $E_{\rm p} \lesssim 500$ keV, but only when assuming a redshift $z \lesssim 0.83$. Deng & Zhang (2014) also found that $\alpha \sim -1.0$ could be achieved if the radiating photosphere has a constant or increasing luminosity. However, they stated that it is difficult to reproduce the observed hard-to-soft evolution under natural conditions.

5. Conclusions

We performed time-resolved spectroscopy for eight energetic, long GRBs observed by *Fermi* GBM during the first five years of its mission. We obtained well constrained BAND spectral parameters and studied their theoretical implications. We showed that even in the bursts with good high-energy statistics above 900 keV, most observed properties can be explained using the Synchrotron Shock Model. We further tested the observed spectra with a synchrotron plus blackbody model using slow- and fast-cooling parametric constraints, and found that the "both" case is consistent with the data, which requires a narrow distribution of the break ratio $E_{\rm b,2}/E_{\rm b,1} < 10$ with a peak at $3.77^{+4.01}_{-1.53}$. The population of p is found to be 2 - 3, in accordance with the expected range. The picture of a "moderately fast-cooling" scenario can also explain the narrow distribution of the break ratio and relax the efficiency issue for the slow-cooling scenario.

Recently, Frontera et al. (2013) reported the result of the time-resolved spectral analysis of four GRBs observed by BATSE and *BeppoSAX*. They found that a specially devised empirical Comptonized model is the best fit model to most of their time-resolved spectra. They also found that using a simple power-law plus blackbody model (PL+BB) does not give fitting results better than the conventional BAND function. This is consistent with the results from the time-resolved GBM GRB catalog (Yu et al. in prep.) that most of the time-resolved spectra are best fitted by a Comptonized model, and only very few spectra are best fitted by PL+BB although they are generally not bad fits. We showed in this paper that the spectral shape $\gtrsim 1$ MeV could be harder than a Comptonized model or simple power-law.

Our results confirmed that while most properties of energetic GRBs can be explained in the conventional theoretical models, the radiative process in GRB prompt emission is complicated and cannot be fully explained by a single distribution of electrons (e.g. due to anisotropic distribution of electron energies or continuous acceleration or photospheric emission). The possibility of a decaying magnetic field which modifies the fast-cooling spectrum is also explored, yielding a magnetic field decay index $0.6 < b < 2.6$ for 77% of the constrained fits. 'However, it is difficult to reconcile the variability of b within bursts with a mechanism where the spectra are shaped by a single large scale decaying magnetic field. Nevertheless, such a field might still exist, but with its impact obscured by more local conditions in the flow.

Acknowledgements. The authors want to thank Frédéric Daigne, Alexander van der Horst, Re'em Sari, Bing Zhang, and the anonymous referee for insightful suggestions. HFY and JG acknowledge support by the DFG cluster of excellence "Origin and Structure of the Universe" (www.universe-cluster.de). The GBM project is supported by the German Bundesministeriums für Wirtschaft und Technologie (BMWi) via the Deutsches Zentrum für Luft und Raumfahrt (DLR) under the contract numbers 50 QV 0301 and 50 OG 0502.

References

Atwood, W. B., Abdo, A. A., Ackermann, M., et al. 2009, ApJ, 697, 1071
Axelsson, M., Baldini, L., Barbiellini, G., et al. 2012, ApJ, 757, L31
Band, D., Matteson, J., Ford, L., et al. 1993, ApJ, 413, 281
Baring, M. G. 2006, Advances in Space Research, 38, 1281
Beloborodov, A. M. 2010, MNRAS, 407, 1033
Beloborodov, A. M. 2011, ApJ, 737, 68
Beloborodov, A. M. 2013, ApJ, 764, 157
Bhat, P. N. 2013, in "Proc. 7th Huntsville GRB Symp.", Huntsville, Apr. 2013, eConf Proc. C1304143
Bissaldi, E., von Kienlin, A., Kouveliotou, C., et al. 2011, ApJ, 733, 97
Bissaldi, E., von Kienlin, A., Lichti, G., et al. 2009, Experimental Astronomy, 24, 47
Boella, G., Butler, R. C., Perola, G. C., et al. 1997, A&AS, 122, 299
Burgess, J. M., Preece, R. D., Baring, M. G., et al. 2011, ApJ, 741, 24
Burgess, J. M., Preece, R. D., Connaughton, V., et al. 2014a, ApJ, 784, 17
Burgess, J. M., Preece, R. D., Ryde, F., et al. 2014b, ApJ, 784, L43
Cash, W. 1979, ApJ, 228, 939
Curran, P. A., Evans, P. A., de Pasquale, M., Page, M. J., & van der Horst, A. J. 2010, ApJ, 716, L135
Daigne, F., Bošnjak, Ž., & Dubus, G. 2011, A&A, 526, A110
Daigne, F. & Mochkovitch, R. 1998, MNRAS, 296, 275
Deng, W. & Zhang, B. 2014, ApJ, 785, 112
Ellison, D. C. & Double, G. P. 2004, Astroparticle Physics, 22, 323
Fishman, G. J., Meegan, C. A., Wilson, R. B., et al. 1989, in Bulletin of the American Astronomical Society, Vol. 21, Bulletin of the American Astronomical Society, 860
Ford, L. A., Band, D. L., Matteson, J. L., et al. 1995, ApJ, 439, 307
Frontera, F., Amati, L., Farinelli, R., et al. 2013, ApJ, 779, 175
Gehrels, N., Chincarini, G., Giommi, P., et al. 2004, ApJ, 611, 1005
Ghirlanda, G., Ghisellini, G., Nava, L., & Burlon, D. 2011, MNRAS, 410, L47
Giannios, D. 2008, A&A, 480, 305
Goldstein, A., Burgess, J. M., Preece, R. D., et al. 2012, ApJS, 199, 19
Goldstein, A., Preece, R. D., Mallozzi, R. S., et al. 2013, ApJS, 208, 21
Goodman, J. 1986, ApJ, 308, L47
Granot, J., Königl, A., & Piran, T. 2006, MNRAS, 370, 1946
Gruber, D., Goldstein, A., von Ahlefeld, V. W., et al. 2014, ApJS, 211, 12
Guiriec, S., Briggs, M. S., Connaugthon, V., et al. 2010, ApJ, 725, 225
Guiriec, S., Connaughton, V., Briggs, M. S., et al. 2011, ApJ, 727, L33
Guiriec, S., Daigne, F., Hascoët, R., et al. 2013, ApJ, 770, 32
Hascoët, R., Daigne, F., Mochkovitch, R., & Vennin, V. 2012, MNRAS, 421, 525
Kaneko, Y., Preece, R. D., Briggs, M. S., et al. 2006, ApJS, 166, 298
Klebesadel, R. W., Strong, I. B., & Olson, R. A. 1973, ApJ, 182, L85
Kouveliotou, C., Meegan, C. A., Fishman, G. J., et al. 1993, ApJ, 413, L101
Liang, E. & Kargatis, V. 1996, Nature, 381, 49
Lithwick, Y. & Sari, R. 2001, ApJ, 555, 540
Lu, R.-J., Hou, S.-J., & Liang, E.-W. 2010, ApJ, 720, 1146

Lu, R.-J., Wei, J.-J., Liang, E.-W., et al. 2012, ApJ, 756, 112
Meegan, C., Lichti, G., Bhat, P. N., et al. 2009, ApJ, 702, 791
Meegan, C. A., Fishman, G. J., Wilson, R. B., et al. 1992, Nature, 355, 143
Mészáros, P., Ramirez-Ruiz, E., Rees, M. J., & Zhang, B. 2002, ApJ, 578, 812
Nava, L., Ghirlanda, G., Ghisellini, G., & Celotti, A. 2011, A&A, 530, A21
Nousek, J. A., Kouveliotou, C., Grupe, D., et al. 2006, ApJ, 642, 389
Paczynski, B. 1986, ApJ, 308, L43
Pe'er, A., Mészáros, P., & Rees, M. J. 2006, ApJ, 642, 995
Peng, Z. Y., Yin, Y., Bi, X. W., et al. 2010, ApJ, 718, 894
Piran, T. 1999, Phys. Rep., 314, 575
Preece, R., Burgess, J. M., von Kienlin, A., et al. 2014, Science, 343, 51
Preece, R. D., Briggs, M. S., Giblin, T. W., et al. 2002, ApJ, 581, 1248
Preece, R. D., Briggs, M. S., Mallozzi, R. S., et al. 1998, ApJ, 506, L23
Preece, R. D., Briggs, M. S., Mallozzi, R. S., et al. 2000, ApJS, 126, 19
Rees, M. J. & Meszaros, P. 1992, MNRAS, 258, 41P
Rees, M. J. & Meszaros, P. 1994, ApJ, 430, L93
Ryan, G., van Eerten, H., MacFadyen, A., & Zhang, B.-B. 2014, arXiv1405.5516
Ryde, F. 2005, ApJ, 625, L95
Sari, R., Piran, T., & Narayan, R. 1998, ApJ, 497, L17
Spitkovsky, A. 2008, ApJ, 682, L5
Summerlin, E. J. & Baring, M. G. 2012, ApJ, 745, 63
Uhm, Z. L. & Zhang, B. 2014, Nature Physics, 10, 351
Vurm, I., Beloborodov, A. M., & Poutanen, J. 2011, ApJ, 738, 77
Yu, H.-F., Preece, R. D., Greiner, J., et al. in prep.
Zhang, B. 2014, International Journal of Modern Physics D, 23, 1430002

Appendix A: Time-Resolved Fitting Results

Table A.1. BAND Parameters for GRB 090902B. The times $t_{\rm start}$ and $t_{\rm stop}$ are relative to the GBM trigger time T_0.

$t_{\rm start}$ (s)	$t_{\rm stop}$ (s)	A (ph s^{-1} cm^{-2} keV^{-1})	$E_{\rm p}$ (keV)	α	β	CSTAT/DOF
0.000	2.325	0.0681±0.0043	521.5±24.1	−0.307±0.039	−4.168±1.980	539.10/478
2.325	4.207	0.0745±0.0043	589.1±27.2	−0.220±0.041	−3.158±0.365	543.25/478
4.207	5.987	0.0780±0.0041	620.5±24.7	−0.197±0.038	−4.367±1.810	547.67/478
5.987	7.173	0.0885±0.0038	959.9±41.2	−0.366±0.030	−4.600±1.470	662.97/478
7.173	7.892	0.1352±0.0054	1421.0±79.2	−0.782±0.019	−5.175±3.080	799.87/478
7.892	8.340	0.2221±0.0093	1631.0±128.0	−1.099±0.016	< −15.53	826.49/478
8.340	8.738	0.2148±0.0100	1811.0±198.0	−1.153±0.016	−3.457±0.674	938.64/478
8.738	9.176	0.2253±0.0095	1801.0±161.0	−1.169±0.015	< −5.522	974.42/478
9.176	9.554	0.2497±0.0112	1737.0±181.0	−1.279±0.015	< −5.696	764.26/478
9.554	9.878	0.3091±0.0163	1082.0±114.0	−1.201±0.018	−3.909±1.280	867.81/478
9.878	10.262	0.2456±0.0123	1171.0±106.0	−1.123±0.018	< −12.89	843.17/478
10.262	10.730	0.2260±0.0095	1588.0±133.0	−1.147±0.016	< −8.822	1000.1/478
10.730	11.116	0.2432±0.0117	1324.0±123.0	−1.108±0.018	−4.184±1.630	779.39/478
11.116	11.633	0.1634±0.0083	1272.0±119.0	−1.110±0.018	< −12.32	805.70/478
11.633	12.270	0.1398±0.0077	1226.0±137.0	−1.140±0.020	−4.258±2.460	712.95/478
12.270	12.982	0.2276±0.0359	137.4±12.3	−0.969±0.062	−2.214±0.106	557.08/478
12.982	13.337	0.6174±0.0740	212.2±11.7	−0.495±0.051	−2.451±0.110	579.38/478
13.337	13.799	0.2969±0.0318	297.8±20.7	−0.808±0.039	−2.751±0.257	475.17/478
13.799	14.247	0.2260±0.0131	668.4±38.6	−0.776±0.025	< −11.92	536.24/478
14.247	14.773	0.1927±0.0117	676.2±42.1	−0.810±0.025	< −9.535	526.75/478
14.773	15.186	0.2159±0.0117	746.0±39.0	−0.665±0.025	< −11.92	552.70/478
15.186	15.682	0.1805±0.0083	999.9±53.3	−0.628±0.024	−4.202±0.990	622.98/478
15.682	16.280	0.1591±0.0114	603.1±46.8	−0.820±0.029	−2.772±0.268	566.78/478
16.280	16.753	0.2031±0.0118	666.4±37.1	−0.683±0.027	−4.580±2.870	586.40/478
16.753	17.418	0.2017±0.0190	366.7±26.3	−0.705±0.039	−2.562±0.185	557.65/478
17.418	18.232	0.1534±0.0144	382.1±29.3	−0.822±0.037	−2.699±0.284	467.21/478
18.232	18.977	0.1515±0.0136	427.2±34.5	−0.907±0.033	−2.916±0.485	484.31/478
18.977	19.575	0.2776±0.0310	278.2±19.1	−0.570±0.049	−2.285±0.096	491.66/478
19.575	19.995	0.3303±0.0322	343.4±22.5	−0.606±0.041	−2.563±0.156	509.15/478
19.995	20.571	0.1728±0.0161	419.3±36.4	−0.869±0.036	−2.450±0.180	509.15/478
20.571	21.148	0.3419±0.0417	217.2±13.7	−0.645±0.050	−2.397±0.119	548.28/478
21.148	21.843	0.3242±0.0417	197.3±11.6	−0.524±0.055	−2.395±0.121	564.19/478
21.843	23.098	0.0832±0.0103	342.9±45.0	−1.146±0.040	−2.283±0.192	565.37/478
23.098	33.792	0.0184±0.0055	134.3±19.5	−1.427±0.061	−2.727±0.780	627.70/478

Table A.2. BAND Parameters for GRB 100724B. The times t_{start} and t_{stop} are relative to the GBM trigger time T_0.

t_{start} (s)	t_{stop} (s)	A (ph s^{-1} cm^{-2} keV^{-1})	E_p (keV)	α	β	CSTAT/DOF
-7.168	10.075	0.0079±0.0005	961.0±129.0	−0.878±0.032	−1.581±0.032	22341./478
10.075	12.503	0.0358±0.0024	570.7±56.3	−0.698±0.043	−1.721±0.035	2558.6/478
12.503	15.016	0.0292±0.0019	662.1±65.9	−0.727±0.040	−1.722±0.037	2459.2/478
15.016	17.022	0.0306±0.0020	1222.0±161.0	−0.877±0.030	−1.790±0.051	1297.9/478
17.022	19.118	0.0301±0.0020	968.7±114.0	−0.793±0.034	−1.744±0.043	1608.2/478
19.118	21.649	0.0249±0.0015	940.3±115.0	−0.882±0.033	−1.648±0.035	3636.6/478
21.649	24.481	0.0262±0.0021	580.1±83.4	−0.847±0.044	−1.580±0.029	4363.6/478
24.481	29.293	0.0208±0.0017	473.6±80.8	−0.862±0.051	−1.494±0.022	10681./478
29.293	38.468	0.0150±0.0017	282.6±49.7	−0.888±0.065	−1.511±0.015	53566./478
38.468	41.089	0.0445±0.0052	286.5±38.3	−0.688±0.067	−1.595±0.024	6721.3/478
41.089	45.942	0.0249±0.0025	298.9±36.6	−0.787±0.058	−1.628±0.020	20827./478
45.942	50.235	0.0184±0.0018	375.9±52.8	−0.890±0.052	−1.636±0.022	20121./478
50.235	55.075	0.0179±0.0017	352.5±44.9	−0.877±0.051	−1.646±0.019	20911./478
55.075	57.006	0.0397±0.0030	525.8±43.7	−0.780±0.039	−1.872±0.030	2355.2/478
57.006	58.742	0.0420±0.0034	499.2±43.7	−0.754±0.041	−1.888±0.028	3499.4/478
58.742	59.914	0.0677±0.0053	436.5±37.5	−0.717±0.044	−1.934±0.043	2615.2/478
59.914	60.965	0.0751±0.0072	364.7±34.8	−0.661±0.052	−1.936±0.049	2171.3/478
60.965	62.298	0.0613±0.0040	457.8±29.2	−0.687±0.040	−1.978±0.021	2335.1/478
62.298	63.162	0.0950±0.0095	454.5±47.1	−0.657±0.048	−1.903±0.050	829.13/478
63.162	64.192	0.0869±0.0099	368.5±38.1	−0.587±0.056	−1.796±0.031	1239.1/478
64.192	65.463	0.0752±0.0075	323.4±30.0	−0.615±0.056	−1.797±0.027	1907.0/478
65.463	66.735	0.0689±0.0056	434.0±39.4	−0.706±0.045	−1.906±0.042	1695.8/478
66.735	67.858	0.0807±0.0082	389.2±38.6	−0.661±0.051	−1.844±0.032	1289.5/478
67.858	69.182	0.0672±0.0064	349.3±32.5	−0.649±0.053	−1.805±0.025	1703.0/478
69.182	70.591	0.0474±0.0051	417.1±56.2	−0.819±0.051	−1.714±0.031	1498.7/478
70.591	72.794	0.0487±0.0061	262.8±30.7	−0.605±0.070	−1.650±0.026	3089.7/478
72.794	74.372	0.0597±0.0061	372.9±37.6	−0.615±0.054	−1.772±0.032	1165.1/478
74.372	75.362	0.0950±0.0105	373.0±36.6	−0.587±0.054	−1.874±0.038	1090.3/478
75.362	76.443	0.1011±0.0112	334.1±31.7	−0.571±0.056	−1.879±0.044	725.08/478
76.443	78.171	0.0513±0.0051	347.2±37.5	−0.759±0.053	−1.791±0.029	1247.7/478
78.171	86.297	0.0109±0.0011	513.8±78.7	−0.982±0.043	−1.634±0.025	15102./478
86.297	123.477	0.0056±0.0038	93.0±49.1	−0.692±0.292	−1.312±0.015	15525./478
123.477	130.458	0.0080±0.0041	143.4±17.6	−0.864±0.083	−2.062±0.134	907.00/478
130.458	142.336	<0.0018	111.8±53.1	−1.168±0.212	−1.842±0.143	1020.7/478

Table A.3. BAND Parameters for GRB 100826A. The times $t_{\rm start}$ and $t_{\rm stop}$ are relative to the GBM trigger time T_0.

$t_{\rm start}$ (s)	$t_{\rm stop}$ (s)	A (ph s^{-1} cm^{-2} keV^{-1})	$E_{\rm p}$ (keV)	α	β	CSTAT/DOF
-2.048	9.547	0.0551±0.0145	144.3±14.5	−0.006±0.160	−1.782±0.055	609.22/356
9.547	11.903	0.0501±0.0099	296.2±42.1	−0.545±0.099	−1.993±0.100	451.52/356
11.903	13.740	0.0650±0.0129	275.8±37.3	−0.543±0.098	−2.032±0.105	412.41/356
13.740	14.495	0.0781±0.0159	323.8±51.6	−0.551±0.100	−1.943±0.094	368.17/356
14.495	15.320	0.0900±0.0178	312.9±47.8	−0.551±0.099	−1.938±0.082	387.25/356
15.320	15.979	0.0629±0.0088	561.2±84.0	−0.814±0.058	−2.813±0.696	349.78/356
15.979	16.622	0.0550±0.0075	693.2±127.0	−0.808±0.061	−2.237±0.195	389.88/356
16.622	17.190	0.0677±0.0093	551.2±81.7	−0.747±0.061	−2.437±0.275	426.53/356
17.190	17.712	0.1054±0.0214	314.5±51.2	−0.582±0.099	−1.891±0.078	359.30/356
17.712	18.294	0.1062±0.0207	328.0±47.5	−0.565±0.092	−2.099±0.120	385.37/356
18.294	18.769	0.1372±0.0264	328.0±45.7	−0.485±0.094	−2.044±0.099	430.26/356
18.769	19.175	0.0908±0.0120	580.0±81.2	−0.696±0.061	−2.502±0.313	397.80/356
19.175	19.580	0.1196±0.0191	433.9±65.9	−0.636±0.077	−2.069±0.102	383.34/356
19.580	19.961	0.0991±0.0137	581.5±92.5	−0.681±0.067	−2.142±0.130	346.77/356
19.961	20.408	0.1155±0.0186	452.9±73.0	−0.676±0.075	−2.070±0.104	359.67/356
20.408	20.825	0.1587±0.0276	353.2±45.8	−0.510±0.085	−2.187±0.120	376.13/356
20.825	21.204	0.1393±0.0220	424.2±57.4	−0.560±0.078	−2.232±0.141	397.45/356
21.204	21.603	0.1282±0.0199	460.3±72.3	−0.696±0.073	−2.130±0.116	375.87/356
21.603	22.059	0.1219±0.0193	424.2±63.6	−0.681±0.074	−2.161±0.130	377.50/356
22.059	22.412	0.1160±0.0161	539.0±81.1	−0.657±0.067	−2.137±0.119	359.72/356
22.412	22.834	0.1335±0.0226	411.0±65.6	−0.604±0.083	−1.952±0.076	391.29/356
22.834	23.301	0.0928±0.0140	549.7±104.0	−0.792±0.067	−1.998±0.099	343.64/356
23.301	23.825	0.0746±0.0112	554.1±96.3	−0.756±0.067	−2.173±0.162	433.43/356
23.825	24.471	0.0710±0.0121	458.0±87.6	−0.754±0.078	−1.938±0.096	402.13/356
24.471	25.169	0.0824±0.0159	355.3±61.4	−0.677±0.088	−1.952±0.095	434.64/356
25.169	25.789	0.0727±0.0137	399.5±79.9	−0.716±0.088	−1.836±0.077	371.05/356
25.789	26.336	0.0907±0.0182	332.9±53.9	−0.636±0.091	−2.004±0.119	424.82/356
26.336	27.189	0.0856±0.0168	309.3±48.8	−0.710±0.088	−2.060±0.120	433.55/356
27.189	28.154	0.0928±0.0210	220.0±33.9	−0.564±0.115	−1.895±0.093	364.10/356
28.154	28.989	0.1055±0.0222	266.2±37.2	−0.628±0.094	−2.128±0.124	438.88/356
28.989	29.888	0.0709±0.0148	316.4±57.6	−0.830±0.086	−2.067±0.133	427.39/356
29.888	31.139	0.0452±0.0098	336.6±75.2	−0.937±0.086	−1.991±0.144	394.69/356
31.139	32.985	0.0408±0.0092	262.2±53.6	−0.812±0.102	−1.837±0.092	399.37/356
32.985	35.735	0.0365±0.0085	228.4±37.4	−0.723±0.103	−1.956±0.126	387.28/356
35.735	37.794	0.0868±0.0321	126.6±21.1	−0.321±0.199	−1.765±0.071	393.57/356
37.794	40.792	0.0496±0.0189	121.6±25.3	−0.542±0.195	−1.722±0.068	407.95/356
40.792	46.181	0.0710±0.0216	117.2±15.9	−0.526±0.154	−1.963±0.094	424.55/356
46.181	60.975	0.0493±0.0150	108.4±13.3	−0.328±0.159	−1.777±0.051	520.17/356
60.975	62.775	0.0614±0.0135	232.6±35.3	−0.768±0.094	−2.094±0.147	442.50/356
62.775	64.610	0.0456±0.0105	258.6±45.7	−0.951±0.082	−2.221±0.236	402.38/356
64.610	70.330	0.0254±0.0057	211.1±35.6	−0.917±0.088	−2.016±0.150	426.15/356
70.330	72.515	0.0279±0.0041	549.0±85.8	−0.968±0.051	< −12.27	410.69/356
72.515	73.736	0.0520±0.0106	346.4±73.5	−0.941±0.080	−2.020±0.136	395.10/356
73.736	76.263	0.0455±0.0106	209.4±31.9	−0.813±0.094	−2.101±0.170	375.69/356
76.263	78.063	0.0561±0.0134	231.3±34.0	−0.889±0.083	−2.472±0.365	377.34/356
78.063	80.235	0.0354±0.0087	263.8±56.3	−1.199±0.070	−2.476±0.547	392.60/356
80.235	83.975	0.1548±0.2100	45.8±12.1	−0.143±0.553	−1.672±0.042	412.44/356
83.975	89.057	0.1167±0.1011	51.3±10.5	−0.384±0.364	−1.805±0.049	386.98/356
89.057	90.011	0.0838±0.0258	169.4±21.9	−1.043±0.082	−3.072±1.090	380.52/356
90.011	91.665	0.1179±0.0450	82.9±11.8	−0.950±0.151	−2.301±0.192	400.87/356
91.665	98.549	0.0659±0.0566	46.9±9.6	−0.552±0.343	−1.857±0.050	440.67/356
98.549	121.856	<1.5170	29.0±6.8	< −1.102	−1.791±0.053	581.38/356

Table A.4. BAND Parameters for GRB 101123A. The times t_{start} and t_{stop} are relative to the GBM trigger time T_0.

t_{start} (s)	t_{stop} (s)	A (ph s^{-1} cm^{-2} keV^{-1})	E_p (keV)	α	β	CSTAT/DOF
38.912	43.589	0.0179±0.0033	497.5±98.7	−0.549±0.101	−1.926±0.100	447.95/356
43.589	44.391	0.0380±0.0033	1635.0±295.0	−0.717±0.048	−2.026±0.114	370.62/356
44.391	44.844	0.0770±0.0104	683.7±129.0	−0.583±0.073	−1.753±0.057	380.88/356
44.844	45.250	0.1016±0.0166	506.6±90.5	−0.606±0.077	−1.884±0.075	372.85/356
45.250	45.628	0.1530±0.0276	374.4±54.5	−0.486±0.088	−1.989±0.086	345.89/356
45.628	45.949	0.1407±0.0267	380.9±67.5	−0.541±0.093	−1.777±0.060	372.09/356
45.949	46.255	0.1001±0.0148	577.7±98.7	−0.728±0.064	−2.132±0.150	399.98/356
46.255	46.552	0.1173±0.0179	544.2±94.3	−0.726±0.067	−2.088±0.125	366.58/356
46.552	46.836	0.1243±0.0206	467.8±75.3	−0.605±0.076	−2.044±0.118	414.08/356
46.836	47.262	0.1339±0.0303	278.5±47.1	−0.702±0.095	−2.040±0.128	404.28/356
47.262	47.831	0.0808±0.0155	416.5±84.7	−0.825±0.077	−2.061±0.144	337.31/356
47.831	48.538	0.0739±0.0137	423.0±84.1	−0.826±0.076	−2.059±0.134	374.63/356
48.538	49.070	0.0923±0.0173	388.3±61.6	−0.679±0.078	−2.255±0.207	382.10/356
49.070	49.701	0.1666±0.0424	198.2±25.3	−0.482±0.114	−2.196±0.167	396.86/356
49.701	50.067	0.1229±0.0174	453.2±50.6	−0.515±0.068	−2.815±0.522	368.62/356
50.067	50.332	0.1673±0.0188	533.5±49.6	−0.582±0.055	−3.884±2.3	364.11/356
50.332	50.600	0.1184±0.0151	616.6±83.3	−0.711±0.056	−2.630±0.367	394.00/356
50.600	51.027	0.1445±0.0320	267.1±41.8	−0.662±0.095	−2.042±0.117	383.01/356
51.027	51.565	0.0824±0.0136	443.1±68.5	−0.915±0.059	−3.471±2.750	368.09/356
51.565	51.904	0.1089±0.0123	648.0±74.4	−0.770±0.049	< −9.740	348.95/356
51.904	52.133	0.1842±0.0233	457.0±42.2	−0.659±0.055	< −14.27	331.89/356
52.133	52.444	0.1727±0.0318	374.4±56.8	−0.641±0.079	−2.204±0.145	412.50/356
52.444	52.701	0.1704±0.0201	518.0±51.0	−0.705±0.052	< −14.90	394.79/356
52.701	53.008	0.1605±0.0253	420.4±56.2	−0.672±0.069	−2.523±0.283	437.42/356
53.008	53.355	0.0999±0.0127	565.9±68.1	−0.737±0.054	−4.167±5.450	401.64/356
53.355	53.681	0.1462±0.0230	425.7±54.1	−0.617±0.068	−2.588±0.329	333.49/356
53.681	54.170	0.0849±0.0157	410.1±71.3	−0.823±0.071	−2.294±0.240	377.17/356
54.170	55.513	0.0225±0.0047	688.9±240.0	−1.053±0.068	−2.049±0.248	394.51/356
55.513	55.962	0.1402±0.0264	346.1±51.1	−0.663±0.081	−2.230±0.161	419.37/356
55.962	56.334	0.0982±0.0124	559.1±60.4	−0.630±0.057	−7.559±264.0	357.26/356
56.334	56.672	0.1198±0.0194	431.7±60.8	−0.708±0.067	−2.483±0.324	346.27/356
56.672	58.101	0.0776±0.0235	199.9±32.8	−0.972±0.093	−2.768±0.627	430.97/356
58.101	62.873	0.0291±0.0105	171.3±42.3	−0.865±0.149	−1.996±0.187	449.63/356
62.873	67.584	0.2631±1.4600	68.4±43.5	< −1.497	−1.418±0.111	489.31/356
81.920	89.903	0.0113±0.0025	568.6±175.0	−1.146±0.069	< −17.00	518.16/356
89.903	92.126	0.0323±0.0090	288.3±53.7	−0.946±0.084	−3.685±5.650	419.32/356
92.126	93.570	0.0327±0.0095	283.1±62.0	−0.968±0.090	−2.350±0.504	466.08/356
93.570	94.965	0.0610±0.0217	140.1±31.2	−0.902±0.146	−2.005±0.173	360.96/356
94.965	100.352	0.0131±0.0087	109.2±50.4	−0.925±0.281	−1.778±0.142	441.31/356
140.288	143.695	0.0172±0.0051	407.7±149.0	−1.208±0.080	−2.602±1.250	373.85/356
143.695	145.029	0.0200±0.0050	537.8±161.0	−1.095±0.069	−2.940±2.800	388.75/356
145.029	146.541	0.0360±0.0137	158.5±42.3	−0.944±0.142	−1.936±0.187	375.53/356
146.541	149.288	0.0444±0.0203	109.1±26.4	−0.847±0.192	−1.997±0.176	393.57/356
149.288	155.648	<0.0793	55.3±19.2	−0.435±0.982	−1.746±0.132	365.35/356

Table A.5. BAND Parameters for GRB 120526A. The times $t_{\rm start}$ and $t_{\rm stop}$ are relative to the GBM trigger time T_0.

$t_{\rm start}$ (s)	$t_{\rm stop}$ (s)	A (ph s^{-1} cm^{-2} keV^{-1})	$E_{\rm p}$ (keV)	α	β	CSTAT/DOF
-2.048	3.367	0.0144±0.0023	625.6±100.0	−0.610±0.145	< −8.973	277.98/239
3.367	5.382	0.0430±0.0069	457.2±57.8	−0.647±0.128	< −12.32	248.49/239
5.382	7.254	0.0339±0.0041	720.7±79.8	−0.533±0.122	< −10.83	256.79/239
7.254	8.973	0.0262±0.0030	1389.0±221.0	−0.893±0.083	< −6.327	302.93/239
8.973	11.365	0.0214±0.0032	865.8±203.0	−0.954±0.106	< −5.560	288.98/239
11.365	13.269	0.0340±0.0042	711.4±88.2	−0.630±0.118	< −11.92	236.42/239
13.269	15.565	0.0224±0.0027	954.3±144.0	−0.521±0.129	−2.691±0.380	271.67/239
15.565	16.889	0.0220±0.0029	1463.0±369.0	−0.724±0.113	−2.174±0.194	263.50/239
16.889	18.729	0.0288±0.0034	1224.0±198.0	−0.894±0.090	< −6.337	264.96/239
18.729	20.182	0.0334±0.0042	1100.0±236.0	−0.911±0.098	−2.885±0.660	248.03/239
20.182	22.412	0.0302±0.0044	683.2±132.0	−0.693±0.134	−2.410±0.271	214.16/239
22.412	24.484	0.0214±0.0028	984.4±163.0	−0.698±0.117	< −6.364	241.56/239
24.484	26.325	0.0300±0.0037	936.3±158.0	−0.768±0.109	−3.186±0.976	234.93/239
26.325	28.016	0.0331±0.0042	781.7±114.0	−0.743±0.108	< −11.92	247.35/239
28.016	29.555	0.0278±0.0035	1119.0±238.0	−0.791±0.108	−2.533±0.347	285.22/239
29.555	30.980	0.0337±0.0052	640.2±109.0	−0.653±0.129	−3.159±1.240	257.64/239
30.980	33.168	0.0298±0.0039	746.7±117.0	−0.695±0.125	−3.105±0.903	285.57/239
33.168	34.993	0.0280±0.0042	853.7±219.0	−0.918±0.112	−2.499±0.407	246.47/239
34.993	36.553	0.0366±0.0062	697.4±204.0	−0.994±0.115	−2.269±0.253	255.41/239
36.553	37.691	0.0362±0.0079	475.6±109.0	−0.991±0.120	< −9.537	246.99/239
37.691	39.667	0.0253±0.0037	821.6±166.0	−0.825±0.115	−3.497±2.140	215.69/239
39.667	41.306	0.0374±0.0061	532.0±86.7	−0.813±0.119	< −14.64	242.91/239
41.306	42.977	0.0404±0.0074	466.1±77.8	−0.757±0.131	−3.940±4.880	204.96/239
42.977	44.596	0.0452±0.0110	342.3±56.5	−0.771±0.141	< −5.606	240.63/239
44.596	46.530	0.0407±0.0083	395.0±62.2	−0.781±0.132	< −14.90	253.36/239
46.530	56.166	0.0064±0.0047	<227.1	−1.568±0.307	−1.966±0.374	298.50/239
56.166	67.584	<0.0052	<21.2	< −1.847	−1.963±0.212	301.17/239

Table A.6. BAND Parameters for GRB 130427A. The times t_{start} and t_{stop} are relative to the GBM trigger time T_0.

t_{start} (s)	t_{stop} (s)	A (ph s^{-1} cm^{-2} keV^{-1})	E_p (keV)	α	β	CSTAT/DOF
-0.064	0.145	0.0821±0.0080	1246.0±126.0	−0.386±0.081	−2.916±0.359	1489.3/357
0.145	0.214	0.1936±0.0197	918.8±73.1	−0.116±0.089	−3.719±0.799	1275.0/357
0.214	0.268	0.3744±0.0374	764.6±62.0	−0.363±0.074	−4.031±1.280	1246.8/357
0.268	0.313	0.4275±0.0506	657.9±63.1	−0.319±0.085	−3.400±0.702	1168.7/357
0.313	0.358	0.5104±0.0558	569.5±42.7	−0.332±0.078	−4.889±3.570	1163.6/357
0.358	0.398	0.4528±0.0510	734.1±75.3	−0.560±0.070	−3.750±1.090	1169.3/357
0.398	0.434	0.7357±0.1020	486.6±47.5	−0.593±0.075	−3.979±1.580	1115.3/357
0.434	0.472	0.5783±0.0660	617.0±60.7	−0.610±0.066	< −11.92	1119.4/357
0.472	0.505	0.5876±0.0804	572.7±69.1	−0.676±0.072	−3.286±0.834	1090.3/357
0.505	0.541	0.9841±0.2210	319.3±42.3	−0.466±0.111	−2.721±0.281	1098.2/357
0.541	0.575	0.6740±0.1011	465.0±53.0	−0.647±0.077	−3.512±1.050	1100.0/357
0.575	0.614	0.8132±0.1500	379.0±47.8	−0.593±0.089	−2.949±0.408	1113.6/357
0.614	0.656	0.4534±0.0718	505.2±65.4	−0.800±0.070	−3.815±2.120	1107.9/357
0.656	0.696	0.5599±0.0885	423.0±44.6	−0.726±0.072	< −6.620	1089.5/357
0.696	0.736	0.5940±0.1160	366.3±50.1	−0.762±0.087	−3.075±0.656	1123.8/357
0.736	0.780	0.4775±0.1011	383.8±65.1	−0.746±0.095	−2.593±0.350	1170.2/357
0.780	0.824	0.6696±0.1150	339.6±32.5	−0.732±0.077	< −9.537	1075.6/357
0.824	0.870	0.4616±0.0926	348.3±43.1	−0.813±0.078	< −9.537	1040.5/357
0.870	0.927	0.8204±0.2170	244.9±32.2	−0.686±0.108	−3.027±0.448	1008.3/357
0.927	0.994	0.6554±0.1690	234.1±28.2	−0.696±0.104	−3.118±0.554	1156.6/357
0.994	1.064	0.5467±0.1660	210.9±33.9	−0.732±0.132	−2.504±0.252	1107.2/357
1.064	1.147	0.4542±0.1370	204.3±31.1	−0.766±0.126	−2.591±0.311	1168.0/357
1.147	1.226	0.9292±0.3080	162.6±19.5	−0.489±0.154	−2.652±0.261	1155.7/357
1.226	1.300	0.9699±0.2980	169.2±13.3	−0.577±0.109	< −7.937	1052.7/357
1.300	1.378	0.8825±0.2450	182.0±14.9	−0.660±0.100	< −5.563	1102.9/357
1.378	1.447	1.3581±0.4850	144.9±13.9	−0.400±0.150	−3.036±0.384	1034.1/357
1.447	1.529	0.5947±0.1870	176.2±18.9	−0.663±0.123	−3.338±0.738	1125.5/357
1.529	1.619	0.5603±0.1870	170.0±15.6	−0.670±0.112	< −4.840	1127.0/357
1.619	1.708	0.8494±0.3490	131.1±10.0	−0.591±0.126	−5.137±5.110	1071.8/357
1.708	1.795	0.5043±0.1810	148.3±16.4	−0.632±0.140	−2.950±0.470	1144.4/357
1.795	1.903	1.0900±0.4041	129.2±10.3	−0.493±0.137	−3.475±0.607	1103.9/357
1.903	2.002	0.6567±0.2420	133.3±13.8	−0.613±0.143	−2.994±0.482	1120.9/357
2.002	2.123	0.8216±0.3150	123.5±11.7	−0.600±0.143	−3.164±0.519	1116.5/357
2.123	2.249	0.7220±0.3370	102.8±12.0	−0.344±0.218	−2.675±0.320	1145.5/357
2.249	2.405	0.5713±0.2600	119.9±9.0	−0.660±0.128	< −6.759	1165.1/357
2.405	2.613	0.7771±0.3810	99.5±7.5	−0.748±0.143	−4.253±1.560	1255.3/357
2.613	2.752	<1.4110	87.3±6.5	−0.302±0.222	−4.909±3.920	1049.3/357

Table A.7. BAND Parameters for GRB 130504C. The times $t_{\rm start}$ and $t_{\rm stop}$ are relative to the GBM trigger time T_0.

$t_{\rm start}$ (s)	$t_{\rm stop}$ (s)	A (ph s^{-1} cm^{-2} keV^{-1})	$E_{\rm p}$ (keV)	α	β	CSTAT/DOF
-6.144	14.601	0.0074±0.0008	969.0±180.0	−0.892±0.049	−2.236±0.208	593.56/359
14.601	15.059	0.0640±0.0071	952.5±164.0	−0.784±0.057	−2.420±0.259	388.66/359
15.059	15.467	0.0539±0.0049	2096.0±454.0	−0.945±0.041	−2.312±0.261	383.17/359
15.467	15.851	0.1054±0.0126	681.7±103.0	−0.732±0.064	−2.311±0.169	368.60/359
15.851	16.140	0.1040±0.0108	959.4±158.0	−0.824±0.052	−2.388±0.220	372.68/359
16.140	16.485	0.1134±0.0170	565.5±101.0	−0.757±0.073	−2.122±0.131	358.14/359
16.485	16.926	0.0876±0.0120	596.3±104.0	−0.813±0.067	−2.210±0.177	414.67/359
16.926	17.368	0.0700±0.0087	727.6±114.0	−0.911±0.053	−3.828±3.170	418.61/359
17.368	18.042	0.0528±0.0080	586.7±112.0	−0.853±0.068	−2.246±0.232	459.53/359
18.042	18.791	0.0594±0.0103	522.2±120.0	−1.011±0.068	−2.189±0.217	380.92/359
18.791	20.215	0.0354±0.0067	487.2±121.0	−1.025±0.073	−2.169±0.238	340.56/359
20.215	24.224	0.0283±0.0067	245.2±49.0	−0.834±0.109	−1.954±0.130	437.97/359
24.224	25.900	0.0468±0.0112	266.8±55.3	−0.933±0.100	−2.079±0.165	422.51/359
25.900	27.775	0.0189±0.0056	300.3±105.0	−1.204±0.096	−2.016±0.276	399.99/359
27.775	28.549	0.0482±0.0089	517.4±124.0	−1.142±0.063	−2.707±0.891	449.85/359
28.549	28.831	0.1072±0.0143	793.9±190.0	−1.011±0.058	−2.103±0.151	420.52/359
28.831	29.323	0.0781±0.0139	538.3±141.0	−0.999±0.074	−2.022±0.130	428.27/359
29.323	30.661	0.0274±0.0046	758.2±222.0	−1.133±0.059	−2.451±0.566	433.24/359
30.661	30.978	0.1087±0.0164	552.3±93.0	−0.686±0.076	−2.160±0.147	399.00/359
30.978	31.173	0.1219±0.0150	951.2±196.0	−0.818±0.059	−2.054±0.124	354.79/359
31.173	31.397	0.1399±0.0207	640.3±131.0	−0.818±0.070	−2.024±0.106	404.81/359
31.397	31.654	0.1717±0.0338	376.4±72.8	−0.852±0.085	−2.142±0.148	356.74/359
31.654	32.002	0.1825±0.0460	237.5±44.7	−0.766±0.117	−2.022±0.117	389.46/359
32.002	32.962	0.0626±0.0172	217.8±66.2	−0.990±0.132	−1.812±0.095	440.69/359
32.962	49.001	0.0522±0.0785	44.9±17.8	−0.553±0.602	−1.718±0.044	784.55/359
49.001	51.264	0.1290±0.1560	66.4±23.7	−0.234±0.542	−1.584±0.046	382.04/359
51.264	52.063	0.6384±1.0200	53.7±15.7	−0.189±0.688	−1.603±0.046	388.96/359
52.063	63.008	<1.0260	29.5±8.3	−0.475±1.250	−1.771±0.042	670.35/359
63.008	64.051	0.0517±0.0100	429.3±88.0	−1.060±0.069	−2.845±1.050	407.86/359
64.051	64.571	0.0582±0.0099	693.2±196.0	−1.172±0.058	−2.556±0.564	393.54/359
64.571	66.126	0.0371±0.0088	349.0±75.8	−1.232±0.067	< −5.742	423.05/359
66.126	67.813	0.0287±0.0073	344.8±84.0	−1.137±0.079	−2.623±0.944	399.31/359
67.813	69.496	0.0292±0.0063	463.6±138.0	−1.182±0.073	−2.324±0.441	467.87/359
69.496	69.836	0.0896±0.0105	725.0±88.0	−0.743±0.056	< −8.680	372.08/359
69.836	70.212	0.1048±0.0141	553.5±73.1	−0.834±0.060	−3.928±3.460	369.74/359
70.212	70.748	0.1316±0.0328	243.4±40.1	−0.724±0.112	−2.167±0.156	363.61/359
70.748	76.011	0.0163±0.0054	235.3±43.6	−1.217±0.078	< −7.767	557.39/359
76.011	78.210	0.0354±0.0115	160.4±51.4	−1.229±0.130	−2.021±0.185	373.22/359
78.210	121.856	< 0.0177	<35.0	−0.898±1.300	−1.684±0.040	1483.3/359

Table A.8. BAND Parameters for GRB 130606B. The times t_{start} and t_{stop} are relative to the GBM trigger time T_0.

t_{start} (s)	t_{stop} (s)	A (ph s^{-1} cm^{-2} keV^{-1})	E_p (keV)	α	β	CSTAT/DOF
-3.072	8.039	0.0406±0.0034	314.8±19.8	−0.561±0.046	−2.012±0.048	592.26/476
8.039	9.019	0.1460±0.0139	370.0±31.6	−0.730±0.044	−2.092±0.064	515.85/476
9.019	9.424	0.1393±0.0070	1951.0±234.0	−1.011±0.021	−2.173±0.107	569.35/476
9.424	9.815	0.1949±0.0139	699.7±72.4	−0.846±0.033	−2.018±0.062	569.74/476
9.815	10.220	0.2004±0.0145	672.6±69.5	−0.846±0.033	−2.005±0.059	539.28/476
10.220	10.764	0.1765±0.0146	507.0±48.0	−0.848±0.036	−2.175±0.082	531.91/476
10.764	11.459	0.1997±0.0205	325.2±26.5	−0.686±0.048	−2.106±0.065	550.81/476
11.459	12.253	0.1464±0.0132	415.6±37.5	−0.808±0.040	−2.154±0.081	539.34/476
12.253	12.859	0.1434±0.0107	651.6±70.3	−0.887±0.033	−2.016±0.059	526.98/476
12.859	13.366	0.2035±0.0156	588.3±64.5	−0.859±0.036	−1.931±0.046	640.58/476
13.366	13.791	0.1857±0.0129	841.1±108.0	−0.962±0.030	−1.922±0.053	534.27/476
13.791	14.244	0.1794±0.0163	582.8±95.4	−0.992±0.039	−1.749±0.038	514.99/476
14.244	14.643	0.1721±0.0118	1066.0±188.0	−1.131±0.027	−1.880±0.057	512.53/476
14.643	15.140	0.1476±0.0109	974.4±181.0	−1.190±0.027	−1.945±0.069	508.88/476
15.140	15.815	0.1257±0.0093	839.6±146.0	−1.279±0.025	−2.154±0.111	556.16/476
15.815	16.659	0.1009±0.0076	732.4±103.0	−1.327±0.024	−3.402±1.230	521.86/476
16.659	17.717	0.0904±0.0094	409.8±58.2	−1.402±0.029	−2.917±0.751	546.90/476
17.717	19.180	0.0648±0.0064	457.8±65.5	−1.418±0.027	< −4.091	536.98/476
19.180	26.218	0.0566±0.0115	63.0±6.1	−1.419±0.078	−2.290±0.085	568.75/476
26.218	36.930	0.0266±0.0042	124.2±18.0	−1.316±0.062	−2.010±0.068	725.95/476
36.930	38.530	0.0848±0.0078	392.3±33.1	−0.938±0.036	−2.682±0.290	591.78/476
38.530	40.034	0.1075±0.0106	330.0±25.9	−0.821±0.042	−2.380±0.128	547.79/476
40.034	41.440	0.2016±0.0274	175.3±11.3	−0.691±0.060	−2.374±0.109	531.31/476
41.440	43.824	0.1237±0.0176	165.6±9.2	−0.858±0.049	−2.774±0.222	446.06/476
43.824	46.694	0.0996±0.0167	153.8±7.5	−0.885±0.047	−3.717±0.974	531.36/476
46.694	49.917	0.1140±0.0179	130.0±7.6	−0.648±0.067	−2.360±0.111	571.19/476
49.917	50.937	0.1577±0.0173	274.3±19.5	−0.763±0.046	−2.476±0.144	516.05/476
50.937	51.685	0.2721±0.0325	214.4±13.0	−0.534±0.055	−2.285±0.085	497.29/476
51.685	52.584	0.2729±0.0332	211.8±11.0	−0.604±0.049	−2.789±0.177	569.27/476
52.584	54.244	0.1599±0.0212	186.7±10.7	−0.708±0.053	−2.617±0.162	574.81/476
54.244	56.959	0.1294±0.0185	156.2±8.9	−0.739±0.057	−2.570±0.161	579.22/476
56.959	77.824	0.0809±0.0246	63.0±4.2	−0.590±0.129	−2.309±0.072	1006.3/476

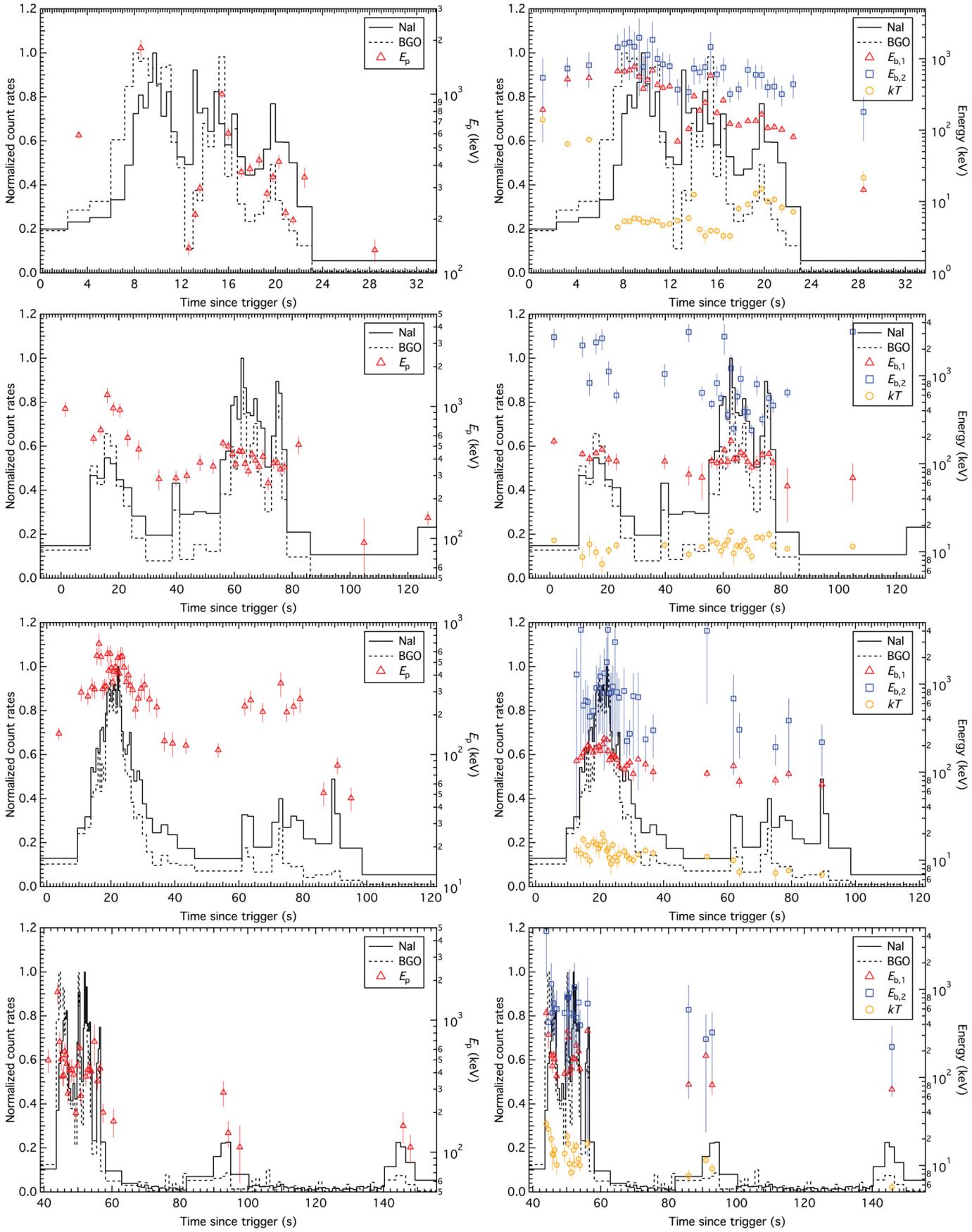


Fig. A.1. Panels from top to bottom: light curves of GRB 090902B, GRB 100724B, GRB 100826A, and GRB 101123A with the evolutions of constrained E_p, $E_{b,1}$, $E_{b,2}$, and kT overlaid.

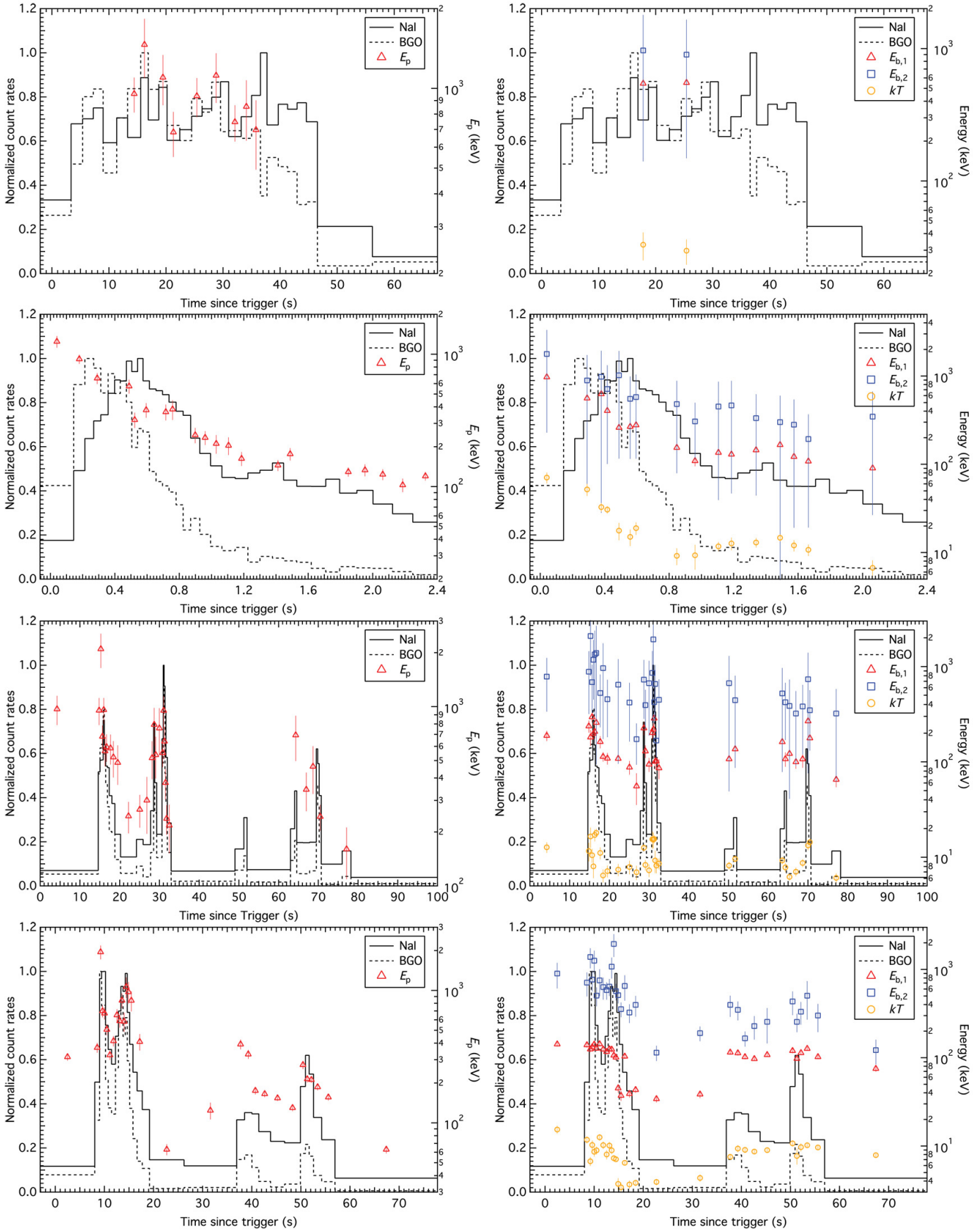


Fig. A.2. Panels from top to bottom: light curves of GRB 120526A, GRB 130427A, GRB 130504C, and GRB 130606B with the evolutions of constrained E_p, $E_{b,1}$, $E_{b,2}$, and kT overlaid.